Verification and validation of complex terrain CFD for wind resource assessment

Louis Naets

DTU Wind-M-0984
July 2025

Author:
Louis Naets

Title:
Verification and validation of complex terrain CFD for wind resource assessment

DTU Wind-M-0984
July 2025

ECTS: 45

Education: Master of Science

Supervisor(s):

Rogier Ralph Floors
Paul van der Laan
DTU Wind & Energy Systems

Simon Watson
TU Delft

Remarks:
This report is submitted as partial fulfillment of the requirements for graduation in the above education at the Technical University of Denmark.

DTU Wind & Energy Systems is a department of the Technical University of Denmark with a unique integration of research, education, innovation and public/private sector consulting in the field of wind energy. Our activities develop new opportunities and technology for the global and Danish exploitation of wind energy. Research focuses on key technical-scientific fields, which are central for the development, innovation and use of wind energy and provides the basis for advanced education at the education.

Technical University of Denmark Department of Wind and Energy Systems Frederiksborgvej 399
4000 Roskilde
Denmark
www.wind.dtu.dk

ABSTRACT

Accurate modelling of wind flow in complex terrain remains a significant challenge in wind resource assessment. Traditional linear models, such as those used in Wind Atlas Analysis and Application Program (WAsP), often fail to capture non-linear effects like recirculation, separation, and stability-driven phenomena typical of steep or mountainous sites. Computational Fluid Dynamics (CFD) methods based on Reynolds-Averaged Navier–Stokes (RANS) equations offer improved accuracy but must be carefully verified and validated for reliability. This thesis evaluates the predictive accuracy of steady-state RANS simulations using PyWakeEllipSys against field measurements from the Perdigão campaign, characterised by complex double-ridge terrain. Three atmospheric stability regimes (stable, neutral, unstable) were simulated, employing various turbulence closures, including standard k–ε and Monin–Obukhov-based models (k–ε–MO). Grid convergence studies ensured robust simulation accuracy at turbine-relevant heights. Results indicate that unstable conditions are modelled most effectively, particularly in predicting terrain-induced speed-up and turbulence intensity profiles. Stable conditions were reasonably well captured in turbulence intensity and flow patterns but showed consistent underprediction of speed-up due to overly persistent recirculation zones. Neutral conditions exhibited inconsistent accuracy across all metrics. Wind direction variability, especially bimodal flow patterns observed in the valley, was not captured by steady-state RANS, highlighting limitations in representing time-dependent, thermally driven flow mechanisms. The outcomes reinforce that steady-state RANS simulations, particularly when stability-adjusted turbulence models are employed, provide strong predictive capabilities for wind resource assessments in complex terrain, although inherent limitations related to transient phenomena must be acknowledged.

ACKNOWLEDGMENTS

I would like to thank my supervisors Paul van der Laan, Simon Watson, and Rogier Floors for their guidance and trust throughout this thesis. From the very beginning, they gave me the freedom to shape the project around my own interests, while always being there when I needed direction. Whenever I got stuck, their support helped me see a clear path forward. I'm especially grateful for the time they made for me in their busy schedules, for asking the right questions, and for helping me bring this work to completion.

It is often said that your closest friends shape who you become. I had the honour of growing into adulthood alongside my friends at Préjardin, friends who are now scattered across the globe, each pursuing their own path. Still, they remain a constant presence, through thick and thin. Hanlin, Toon, Anton, Camille, Seba, Bo, Boris, and Korneel. Thank you for showing me what ambition looks like, for sharing routines and habits that still ground me today, and for setting a standard of friendship built on trust, respect and shared curiosity. Those early days shaped more than I realised at the time.

Finally, I'd like to thank my family for always standing behind my choices, even when they took me far from home. Your steady support and belief in me made it easier to keep moving forward. Whether it was a quiet check-in or an enthusiastic question about my progress, you reminded me that this work didn't exist in a vacuum.

CONTENTS

LIST OF FIGURES

LIST OF TABLES

LIST OF SYMBOLS

c	Smoothing exponent in radial terrain transition [-]
d	Displacement height [m]
f_0	Extrapolated solution at zero grid spacing [–]
f_P	Length scale limiter [-]
g	Gravitational acceleration [m/s²]
g_1, g_2	First- and second-order error coefficients [–]
h	Terrain elevation [m]
m	Terrain slope [-]
n	Number of samples [-]
p	Pressure [Pa]
r	Radial coordinate [m]
s	Horizontal streamwise coordinate [m]
t	Time [s]
u	Streamwise wind component [m/s]
$\bar{u}$	Time-averaged streamwise velocity [m/s]
u'	Fluctuation of u from mean [m/s]
u_*	Friction velocity [m/s]
v	Spanwise wind component [m/s]
v'	Fluctuation of v from mean [m/s]
w	Vertical wind component [m/s]
w'	Fluctuation of w from mean [m/s]
z	Height above ground level [m]
z_0	Surface roughness length [m]

A	Terrain area [m²]
B	Buoyancy source term in the k–ε–MOB model [m²/s³]
C_μ	Turbulence model constant for eddy viscosity [-]
D	Rotor diameter [m]
H	Height of hill [m]
L	Obukhov length [m]
L_{xy}	Horizontal domain width [m]
N_{CPU}	Number of CPU cores [-]
P_k	Production of turbulent kinetic energy [m²/s³]
Ri_b	Bulk Richardson number [-]
S_{ij}	Mean strain-rate tensor [1/s]
U	Mean wind speed [m/s]
U_0	Reference wind speed at flat upstream location [m/s]
$U(z)$	Wind speed at height z [m/s]
$U(z_P)$	Wind speed at the first cell centre height z_P [m/s]
x, y	Cartesian horizontal coordinates [m]

Γ	Dry adiabatic lapse rate [K/m]
δ_{ij}	Kronecker delta [-]
ΔS	Relative speed-up factor [-]
Δz	Vertical distance to the wall [m]
ε	Turbulence dissipation rate [m²/s³]
$\epsilon(h)$	Discretisation error at grid spacing h [–]
ζ	Stability parameter ($\zeta = z/L$) [-]
θ	Potential temperature [K]
θ_v	Virtual potential temperature [K]
κ	von Kármán constant [-]
ν	Kinematic viscosity [m²/s]
ν_t	Eddy viscosity [m²/s]
ρ	Air density [kg/m³]
σ	Shear parameter [-]
$\tilde{\sigma}$	Normalised shear [-]
σ_u	Standard deviation of u [m/s]
τ_w	Wall shear stress [Pa]
ϕ_m, ϕ_ε	MOST non-dimensional gradient functions [-]
ψ_m	MOST correction function [-]
Ψ_m	Integrated stability correction function for momentum [-]

LIST OF ABBREVIATIONS

ABL	Atmospheric Boundary Layer
ASL	Atmospheric Surface Layer
CFD	Computational Fluid Dynamics
DEM	Digital Elevation Model
DNS	Direct Numerical Simulation
DTU	Technical University of Denmark
ETC	European Turbine Category
IBL	Internal Boundary Layer
IOP	Intensive Observation Period
LES	Large Eddy Simulation
LIDAR	Light Detection and Ranging
LST	Local Solar Time
MOST	Monin–Obukhov Similarity Theory
NaN	Missing Value
NASADEM	NASA Digital Elevation Model
NCAR	National Center for Atmospheric Research
NEWA	New European Wind Atlas
RANS	Reynolds-Averaged Navier–Stokes
RIX	Ruggedness Index
SEM	Standard Error of the Mean
TI	Turbulence Intensity
TKE	Turbulent Kinetic Energy
UTM	Universal Transverse Mercator
WAsP	Wind Atlas Analysis and Application Program
WRF	Weather Research and Forecasting (model)
WTG	Wind Turbine Generator

1 INTRODUCTION

The study of wind flow over hills, valleys, and other forms of complex topography plays an important role in the global transition to renewable energy [8]. Onshore wind remains one of the most cost-effective sources of clean electricity, with substantial growth projected in the coming years. According to the Global Wind Energy Council, global onshore wind capacity is expected to grow by 827 GW between 2025 and 2030, with a compound annual growth rate of 6.6% [24]. This expansion is driven by demand for reliable, decentralised energy and reinforced by political targets such as the EU Green Deal and China's carbon neutrality goals.

While early wind power development often targeted elevated or coastal sites to exploit stronger and more consistent winds, the industry later prioritised flatter, more accessible terrain due to lower construction costs, simplified logistics, and easier grid integration. However, as many of these prime flat sites with minimal obstacles become saturated or constrained, developers are once again turning to mountainous and forested regions [50]. These locations offer favourable wind conditions and lower land-use conflict but introduce substantial aerodynamic complexity. Elevated terrain can amplify wind speeds through local speed-up effects, boosting energy production if turbines are correctly placed. At the same time, steep slopes, irregular surface roughness, and thermally-driven flows produce separation, recirculation, and increased turbulence, complicating flow prediction and increasing uncertainty in energy yield assessments [62].

Traditional models, such as those integrated in WAsP (Wind Atlas Analysis and Application Program), remain widely used due to their speed and robustness, but perform poorly in complex terrain [29]. These models rely on simplified assumptions that exclude non-linear flow effects and stability-driven mechanisms. In contrast, Computational Fluid Dynamics (CFD) methods based on the Reynolds-Averaged Navier–Stokes (RANS) equations offer a more detailed and physically grounded approach. RANS models resolve mean flow fields and can capture terrain-induced acceleration, separation, and atmospheric stability effects when properly configured. Unlike wind tunnel tests or mesoscale models, CFD can be applied at full scale and high spatial resolution, making it a solid candidate for site-specific flow analysis in complex terrain [8].

While Large Eddy Simulation (LES) and Direct Numerical Simulation (DNS) offer higher fidelity, their computational cost remains prohibitive for wind energy applications over full domains. RANS models sit in the middle of this hierarchy, providing a trade-off between accuracy and feasibility. However, their success depends on the choice of turbulence model, boundary conditions, and stability parametrisation. Moreover, validation against well-characterised datasets remains essential before models can be reliably applied to site development.

PyWakeEllipSys is a Python interface built around the EllipSys3D RANS solver. It connects CFD simulations to the WAsP ecosystem, facilitating terrain-based modelling, stability classification, and post-processing of simulation results.

This thesis contributes to ongoing efforts to reduce uncertainty in wind resource assessment over complex terrain by validating PyWakeEllipSys simulations against observations from the Perdigão field campaign. The site features a double-ridge valley configuration with extensive meteorological mast instrumentation, allowing for detailed evaluation of CFD model performance across stability regimes and flow orientations. The work supports the European TPWind "3% vision" of reducing annual energy production uncertainty to below 3%, a target that requires consistent and accurate flow modelling frameworks [18].

The central research question is:

> *To what extent can RANS-based CFD simulations in PyWakeEllipSys accurately reproduce observed flow conditions over complex terrain?*

This question is addressed through the following sub-questions:

1. How well do simulated speed-up factors, turbulence intensities, and wind directions compare with mast measurements across the ridge–valley system?
2. To what extent are vertical profiles of speed-up, wind direction, and turbulence intensity captured under stable, neutral, and unstable conditions?
3. How can PyWAsP be used to process meteorological and terrain data for simulation and validation?
4. How does the choice of turbulence closure and stability correction affect simulation accuracy across different flow regimes?
5. Which terrain-induced microscale flow phenomena in a 2D valley can be resolved by RANS, and which are fundamentally out of reach?

By addressing these questions, the thesis evaluates both the predictive strength and the limitations of steady-state RANS simulations for wind resource assessment in complex terrain. The analysis focuses not only on validation of mean flow quantities but also on the ability of the model to reproduce full flow structures observed during field campaigns.

The structure of this thesis is as follows. Chapter 2 introduces the theoretical background on boundary-layer flow, terrain-induced effects, and turbulence modelling. Chapter 3 describes the Perdigão field campaign and the validation dataset. Chapter 4 outlines the simulation setup, model configurations, and preprocessing steps. Chapter 5 contains the main results and analysis. Chapter 6 presents a grid resolution study. Chapter 7 summarises the findings and outlines recommendations for future work.

2

BACKGROUND

This chapter provides the theoretical foundation for the work presented in this thesis. It introduces the governing dynamics of boundary-layer flow over complex terrain, with emphasis on surface-layer scaling, terrain-induced flow features, and turbulence generation. The final sections focus on turbulence modelling in CFD, including the assumptions and limitations of RANS-based approaches relevant to this study.

2.1 WIND RESOURCE MODELLING IN COMPLEX TERRAIN

2.1.1 *The Atmospheric Boundary Layer*

The Atmospheric Boundary Layer (ABL) is the lowest part of the atmosphere directly influenced by the Earth's surface, typically extending up to 500–2000 m depending on surface roughness, thermal stratification, and synoptic conditions [23, 54]. Within this layer, momentum, heat, and moisture are exchanged between the surface and the atmosphere through turbulence. Its dynamics are governed by both mechanical and buoyant production of turbulence, making it highly variable in space and time.

The ABL is typically structured into vertical sublayers. Closest to the ground is the surface layer (ASL), where vertical gradients of wind, temperature, and humidity are strongest and where turbulent fluxes are approximately constant with height. Above the ASL lies the logarithmic layer, where wind profiles often follow a near-universal shape under neutral conditions [54].

In a horizontally homogeneous, neutrally stratified ASL, the vertical wind speed profile is commonly approximated by the logarithmic law:

$$U(z) = \frac{u_*}{\kappa} \ln\left(\frac{z}{z_0}\right), \tag{2.1}$$

where $U(z)$ is the horizontal wind speed at height z, u_* is the friction velocity, $\kappa \approx 0.4$ is the von Kármán constant, and z_0 is the surface roughness length [23, 54].

2.1.2 *Surface Roughness*

Surface roughness affects the structure of the atmospheric boundary layer by modulating the momentum exchange between the surface and the flow. The key parameter used to quantify surface-induced drag is the aerodynamic roughness length, z_0, which characterises the height at which the logarithmic wind profile extrapolates to zero velocity under neutral stability conditions [25].

According to the logarithmic law, introduced in Equation 2.1, higher roughness values result in greater momentum loss near the surface, thereby reducing wind speeds in the lower boundary layer and increasing shear.

As shown in Figure 2.1, spatial variability in z_0 introduces horizontal heterogeneity in surface drag. When the surface roughness changes (e.g. from z_0 to z_1), the wind profile must adjust, initiating the formation of an internal boundary layer (IBL). This IBL grows downstream from the transition point, encapsulating the flow that has been modified by the new surface condition. The height of the IBL, denoted h_∞, increases with distance x and determines the depth over which the new roughness affects the flow.

Within the IBL lies the so-called adapted layer, which is the portion of the flow that has fully adjusted to the new surface roughness z_1. In this region, the wind profile again follows a logarithmic shape but with z_1 as the roughness length, contrasting with the upstream region where the profile was based on z_0. The adapted layer thus reflects a fully equilibrated local boundary layer. The transition between the upstream and downstream conditions involves shear deformation, turbulence generation, and vertical mixing, especially within and above the IBL.

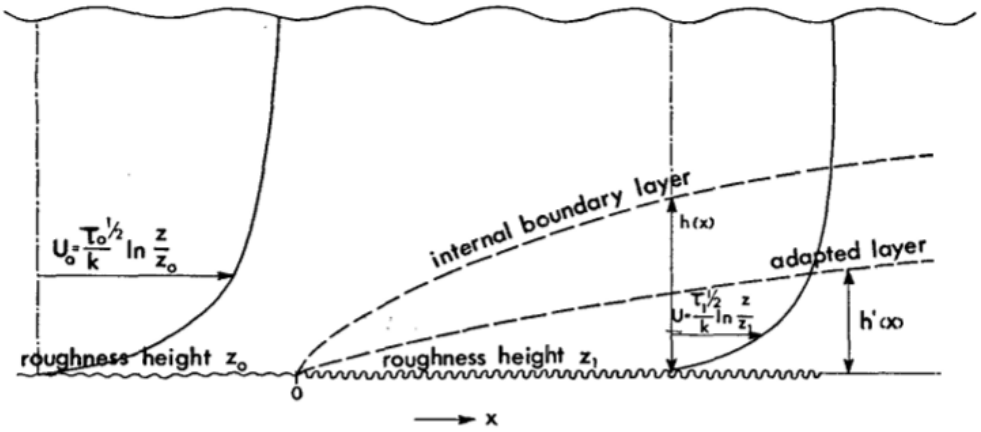

Figure 2.1: Schematic illustration of wind profiles over surfaces with different roughness lengths z_0.[9]

2.1.3 *Orography*

Orography refers to spatial variations in terrain elevation that influence atmospheric flow. In relatively smooth or mildly varying terrain, wind acceleration over hills, commonly known as the speed-up effect, is typically well captured by linearised flow models for moderate terrain slopes. This phenomenon results from the compression of streamlines as the flow is forced over elevated surfaces, leading to an increase in wind speed at the hilltop compared to a reference point upstream at the same height above the surface.
The relative speed-up ΔS is classically defined as [57]:

$$\Delta S = \frac{U(z_{agl})}{U_0(z_{agl})} - 1, \tag{2.2}$$

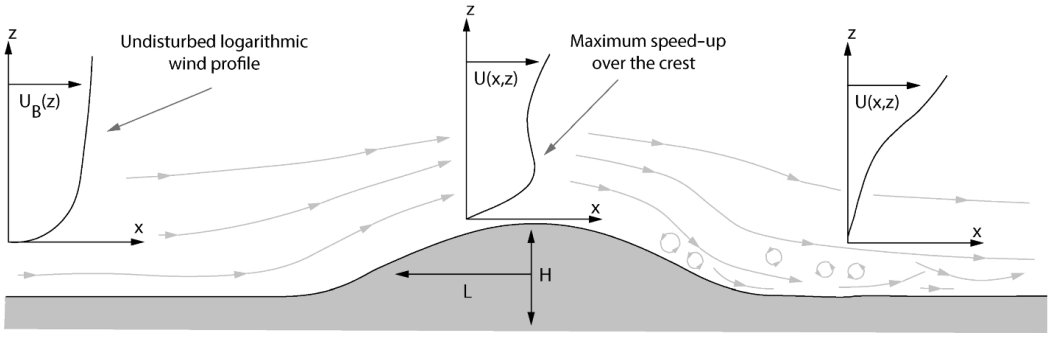

Figure 2.2: speed-up over ideal hill [61].

where $U(z_{agl})$ is the predicted wind speed at a given height above ground level, and $U_0(z_{agl})$ is the reference wind speed at the same height. Following a dimensional analysis by van der Laan et al. (2020), terrain-induced speed-up factors are shown to be independent of the absolute inflow wind speed, provided that the flow remains in the high Reynolds number regime [40].

However, in steep terrains with slopes exceeding 30%, flow separation occurs, resulting in the formation of recirculation zones and wakes. These phenomena introduce significant complexities into the flow, making traditional linear flow models less effective. To quantify terrain steepness, the ruggedness index (RIX) was introduced as a diagnostic metric for the applicability of linearised models such as WAsP. RIX is defined as the fraction of terrain surrounding a site that exceeds a predefined critical slope threshold of around 30%. A RIX value of 0% indicates terrain within the operational assumptions of WAsP, while larger values signal increased likelihood of separated flow [5].

2.1.4 *Turbulence Intensity*

Turbulence is a fundamental characteristic of ASL flows and plays a key role in wind flow modelling over complex terrain. Unlike laminar flow, which is smooth and orderly, turbulent flow is marked by velocity fluctuations, eddies, and energy dissipation across a wide range of scales. Figure 2.3 visualises the difference between laminar and turbulent velocity profiles. In the laminar case, flow accelerates smoothly from the surface through a parabolic profile. In turbulent conditions, however, the instantaneous velocity exhibits highly irregular fluctuations, while the time-averaged velocity profile maintains a much sharper gradient near the surface due to enhanced momentum transport from eddies [48].

The metric for characterising turbulence in the ASL is the turbulence intensity (TI), a dimensionless parameter defined as the ratio of the root mean square of the velocity fluctuations to the mean wind speed over a given averaging period [27]:

$$TI = \frac{\sigma_u}{\overline{U}} \tag{2.3}$$

where σ_u denotes the standard deviation of the streamwise velocity fluctuations, and $\overline{U}$ is the mean streamwise velocity. In practice, σ_u is either derived from high-frequency wind measurements or CFD outputs via turbulence quantities such as the turbulent kinetic

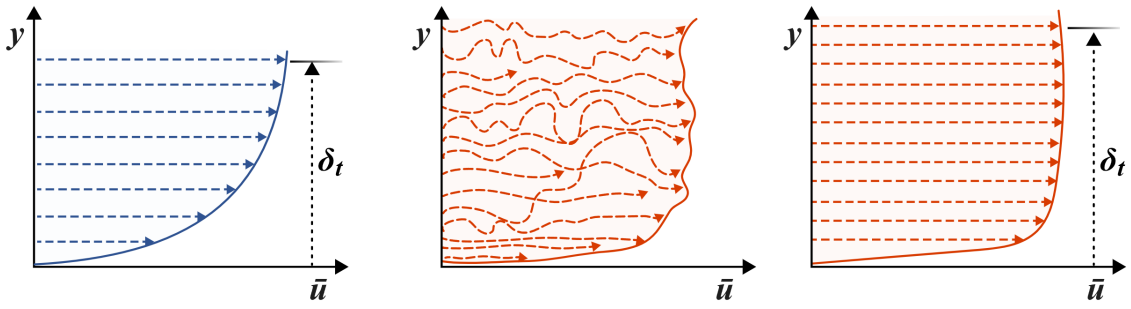

Figure 2.3: Comparison of laminar and turbulent velocity profiles.

energy (k). Assuming isotropic turbulence, where $\overline{u'^2} = \overline{v'^2} = \overline{w'^2}$, this relation simplifies to:

$$\sigma_u = \sqrt{\frac{2}{3}k}, \quad \text{with} \quad k = \frac{1}{2}\left(\overline{u'^2} + \overline{v'^2} + \overline{w'^2}\right) \tag{2.4}$$

This assumption simplifies the connection between k and TI but is often unrealistic in atmospheric boundary layers, especially over complex terrain. Anisotropy increases under stable stratification or in regions with shear, recirculation, or separation [54]. RANS models impose isotropy by design, which can lead to misrepresentation of turbulence magnitudes and transport when compared to LES results [12].

In RANS simulations, inflow conditions are typically defined through k. Since k is derived from TI via $k = \frac{3}{2}(TI \cdot \overline{U})^2$, the specified TI must reflect the total turbulence intensity. However, as a result of said isotropy assumption, standard surface-layer component ratios are applied: $\sigma_v/\sigma_u = 0.8$ and $\sigma_w/\sigma_u = 0.5$, as adopted in the IEC 61400-1 standard [30] and originally measured by Panofsky and Dutton [47]. This yields the approximation:

$$TI_{TKE} \approx \sqrt{\frac{1}{3}\left(1 + 0.8^2 + 0.5^2\right)}\, TI_u \approx 0.8\, TI_u \tag{2.5}$$

This scaling should be applied when converting measured TI for use as a RANS inflow boundary condition. For post-simulation comparison, the TI derived from CFD outputs, typically computed as $\sqrt{2k/3}/\overline{U}$, can be directly compared to measured TI_u if the distinction in definition is acknowledged. [37].

TI also serves as a model validation metric. It reflects how well turbulence production and transport are resolved. Still, caution is needed when interpreting CFD-derived TI, especially in RANS, where isotropy rarely holds in flows over valleys, ridges, or forested slopes [**berg2011**, 4].

2.1.5 *Atmospheric Stability*

Atmospheric stability, governed primarily by the vertical temperature gradient, strongly influences turbulence intensity, wind shear, and vertical momentum exchange within the ABL. Accurate representation of stability effects is therefore essential for reliable wind resource modelling and turbine load analyses [23, 54].

A commonly employed framework for quantifying atmospheric stability is Monin–Obukhov Similarity Theory (MOST), which introduces the Obukhov length (L). MOST defines a dimensionless stability parameter, $\zeta = z/L$, representing the relative influence of buoyant and mechanical turbulence production at height z. The wind speed profile under MOST can be expressed as:

$$U(z) = \frac{u_*}{\kappa}\left[\ln\left(\frac{z}{z_0}\right) - \psi_m\left(\frac{z}{L}\right)\right], \tag{2.6}$$

where $U(z)$ is the mean wind speed at height z, u_* is the friction velocity, $\kappa \approx 0.4$ is the von Kármán constant, z_0 is the aerodynamic roughness length, and $\psi_m(z/L)$ is the stability correction function varying according to stability conditions [54].

A simplified version of stability classification defined through MOST from Sorbjan (2010) is summarised in Table 2.1:

Table 2.1: Stability classification based on the Obukhov stability parameter ζ [53].

Stability Class	**Stability Parameter Range**
Very Unstable	$\zeta < -0.6$
Unstable	$-0.6 \leqslant \zeta < -0.02$
Neutral	$-0.02 \leqslant \zeta \leqslant 0.02$
Stable	$0.02 < \zeta \leqslant 0.6$
Very Stable	$\zeta > 0.6$

Negative values of L indicate unstable conditions, typically during daytime surface heating, promoting strong vertical mixing, reducing wind shear, and resulting in flatter wind profiles. Positive L values correspond to stable conditions, generally occurring at night due to radiative cooling of the surface, suppressing turbulence and increasing wind shear near the ground. Neutral conditions ($|L| \to \infty$) prevail when mechanical turbulence dominates, typically under strong winds or cloudy conditions [23]. These stability regimes and their corresponding wind profiles are illustrated in Figure 2.4.
Alternative stability characterisation methods, such as the Bulk Richardson number (Ri_b) and gradient Richardson number (Ri_g), are also frequently used. These Richardson number-based methods rely on gradients of wind speed and temperature and are computationally simpler, requiring only mean meteorological data at discrete vertical levels.

Comparative studies have assessed the relative merits of MOST and Richardson number approaches in complex terrains. Cantero et al. (2022), for instance, demonstrated that while Ri_b is simpler and more practical in data-scarce situations, it frequently misrepresents local

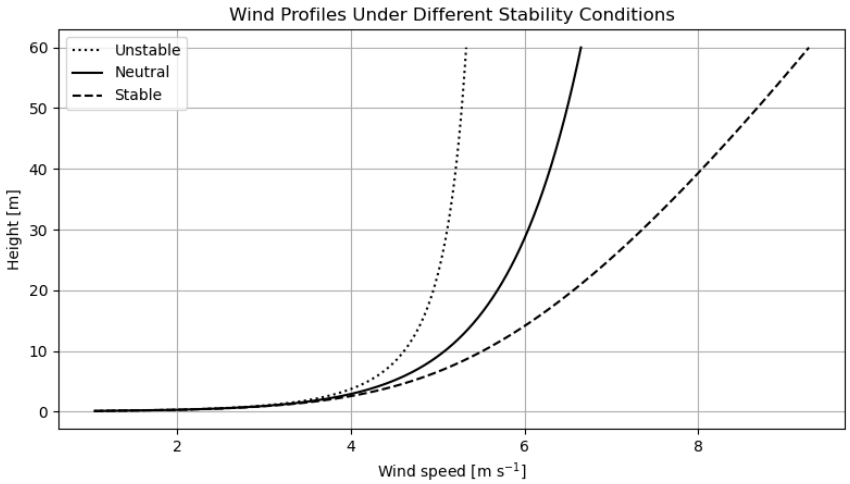

Figure 2.4: Wind speed profiles for different atmospheric stability conditions, highlighting the distinct wind shear characteristics [54].

stability conditions, particularly under stable regimes. Conversely, MOST provides a more robust and precise characterisation of atmospheric stability when high-frequency turbulence data (e.g., sonic anemometer data) are available, despite its underlying assumptions of horizontal homogeneity and stationarity occasionally being violated in complex terrain [11].

2.2 TURBULENCE MODELLING - RANS

The Reynolds-averaged Navier–Stokes (RANS) approach is a widely used method in computational fluid dynamics to model turbulent flows. Instead of solving for the full time-dependent behaviour of turbulence, RANS focuses on the average flow field by separating each flow variable into a mean and a fluctuating component. This allows for practical simulation of turbulent flows by avoiding the need to resolve all small-scale turbulent structures directly.

In wind engineering and atmospheric flow modelling, RANS is frequently used due to its balance between computational cost and accuracy. It enables the prediction of mean wind fields over complex terrain. However, because turbulence is only modelled and not resolved, RANS results depend on the turbulence closure model used. These models attempt to represent the effect of turbulence on the mean flow using additional transport equations or empirical relationships.

2.2.1 *Governing equations of RANS*

The Reynolds-averaged Navier–Stokes equations form the foundation for most computational wind engineering applications involving turbulent flows. They are derived by applying Reynolds decomposition to the unsteady incompressible Navier–Stokes equations, which results in a system that governs the evolution of mean flow quantities.
The incompressible mass conservation equation is given by:

$$\nabla \cdot \bar{\mathbf{u}} = 0, \tag{2.7}$$

where $\bar{\mathbf{u}}$ is the time-averaged velocity vector. This equation states that mass is conserved locally in the flow, meaning that fluid neither accumulates nor disappears at any point in space. This can also be expressed using the Einstein notation as shown in Equation 2.8

$$\frac{\partial u}{\partial x} + \frac{\partial v}{\partial y} + \frac{\partial w}{\partial z} = 0, \quad \frac{\partial u_i}{\partial x_i} = 0 \tag{2.8}$$

Here, u, v, and w represent the velocity components in the streamwise (x), cross-stream (y), and vertical (z) directions, respectively.

Next, the Navier–Stokes equation describes how the velocity field of a fluid evolves due to different forces acting on it. It is essentially Newton's second law applied to a fluid element, stating that changes in momentum are balanced by external forces and internal stresses:

$$\underbrace{\frac{\partial u_i}{\partial t}}_{\text{term I}} + \underbrace{\frac{\partial}{\partial x_j}\left(u_i u_j\right)}_{\text{term II}} = \underbrace{f_i}_{\text{term III}} + \frac{\partial \sigma_{ij}}{\partial x_j}, \quad \sigma_{ij} = \underbrace{-\frac{1}{\rho} p \delta_{ij}}_{\text{term IV}} + \underbrace{\nu\left(\frac{\partial u_i}{\partial x_j} + \frac{\partial u_j}{\partial x_i}\right)}_{\text{term V}} \tag{2.9}$$

Where ρ, p and ν are the density, pressure, and kinematic viscosity of the fluid, respectively. Furthermore, δ_{ij} is the Kronecker delta, which equals 1 when $i = j$ and 0 when $i \neq j$; it is used to isolate diagonal components such as pressure acting in the same direction as the coordinate axis.

The Navier-Stokes Equation 2.9 can be divided into different terms, each representing a different physical process in the flow: Term I describes how the velocity changes with time. Term II accounts for the convective term of transport of momentum, or the transport of momentum by the fluid itself; this is how fast-moving fluid carries momentum into surrounding areas. Term III includes external body forces like gravity or the Coriolis force. Term IV represents pressure forces acting on fluid elements. Term V captures the effects of internal friction (viscosity), which is the diffusion due to viscous dissipation through heat.

As its name suggests, RANS applies Reynolds Averaging to the Navier Stokes equation, separating u_i into a mean component $\bar{u_i}$ and a fluctuating component u_i'

$$u_i = \bar{u}_i + u_i', \quad \overline{u_i'} = 0, \quad \overline{u_i' u_j'} \neq 0 \tag{2.10}$$

Applying Reynolds decomposition to the incompressible Navier–Stokes momentum equation yields:

$$\frac{\partial \bar{u}_i}{\partial t} + \bar{u}_j \frac{\partial \bar{u}_i}{\partial x_j} = -\frac{1}{\rho}\frac{\partial \bar{p}}{\partial x_i} + \nu \frac{\partial^2 \bar{u}_i}{\partial x_j^2} - \frac{\partial \overline{u_i' u_j'}}{\partial x_j} \tag{2.11}$$

This equation describes how the mean velocity field evolves, accounting for pressure gradients, viscous diffusion, and an additional term: the divergence of the Reynolds stress tensor $\overline{u_i' u_j'}$. This last term arises due to averaging the non-linear convective term, and it introduces six new unknowns (one for each independent component of the symmetric Reynolds stress tensor in 3D). When combined with the three velocity components and the

pressure, the system ends up with 10 unknowns but only 4 equations

This mismatch is known as the *closure problem*. Without additional relationships to estimate the Reynolds stresses, the equations cannot be solved; hence, supplementary modelling is required to close the system. This leads to the use of turbulence models. In engineering practice, the most common approach is the eddy viscosity concept, introduced via the Boussinesq approximation:

$$-\overline{u_i' u_j'} = 2\nu_t S_{ij} - \frac{2}{3} k \delta_{ij}, \tag{2.12}$$

where ν_t is the eddy viscosity, k is the turbulent kinetic energy, and S_{ij} is the mean strain-rate tensor:

$$S_{ij} = \frac{1}{2}\left(\frac{\partial \bar{u}_i}{\partial x_j} + \frac{\partial \bar{u}_j}{\partial x_i}\right). \tag{2.13}$$

The eddy viscosity ν_t is modelled using empirical turbulence models, which will be introduced later in this section.

The RANS framework significantly simplifies the full Navier–Stokes equations by reducing the computational cost and making simulations feasible for realistic engineering domains. However, it does so at the expense of resolving fine-scale turbulence and transient flow structures.

2.2.2 *The k-ε Turbulence Model*

The k-ε model, initially introduced by Launder and Spalding (1974) [43], is a widely used RANS turbulence model. It employs two transport equations to represent the turbulence kinetic energy (k) and its dissipation rate (ε). This turbulence model assumes isotropic turbulence, utilising the classical Boussinesq hypothesis to express Reynolds stresses, as described in the PyWakeEllipSys documentation [33]. The governing equations for the standard k-ε turbulence model in their steady-state form are given by:

$$\frac{\partial}{\partial x_j}(U_j k) = \frac{\partial}{\partial x_j}\left[\left(\nu + \frac{\nu_T}{\sigma_k}\right)\frac{\partial k}{\partial x_j}\right] + P_k - \varepsilon, \tag{2.14}$$

$$\frac{\partial}{\partial x_j}(U_j \varepsilon) = \frac{\partial}{\partial x_j}\left[\left(\nu + \frac{\nu_T}{\sigma_\varepsilon}\right)\frac{\partial \varepsilon}{\partial x_j}\right] + \frac{\varepsilon}{k}(C_{\varepsilon 1} P_k - C_{\varepsilon 2}\varepsilon), \tag{2.15}$$

where U_j are the mean velocity components, P_k represents the production rate of turbulent kinetic energy, ν is the kinematic viscosity, and ν_T is the eddy viscosity defined as:

$$\nu_T = C_\mu \frac{k^2}{\varepsilon}, \tag{2.16}$$

with model constants typically set as $C_\mu = 0.09$, $\sigma_k = 1.00$, $\sigma_\varepsilon = 1.30$, $C_{\varepsilon 1} = 1.44$, and $C_{\varepsilon 2} = 1.92$ [43].

2.2.3 *The* k-ε-f_P *Turbulence Model*

The modified k-ε turbulence model, referred to as the k-ε-f_P model, extends the standard k-ε formulation by introducing a limiter function f_P that adjusts the local eddy viscosity based on the mean flow shear. The main objective of this modification is to avoid over-prediction of eddy viscosity in regions with strong velocity gradients, such as the near-wake zone or flow over steep terrain features.

In the standard model, the eddy viscosity is defined as $\nu_T = C_\mu k^2/\varepsilon$, with C_μ constant. This leads to unrealistically high values of ν_T in areas of high shear, artificially enhancing turbulent diffusion and prematurely accelerating wake recovery. This behaviour is well documented in wind turbine wake studies, where the standard model underpredicts velocity deficits behind the first turbine in a row [37].

To resolve this, the k-ε-f_P model replaces the constant C_μ with a shear-dependent term $C_\mu f_P$, where f_P is given by:

$$f_P = \frac{2f_0}{1+\sqrt{1+4f_0(f_0-1)(\sigma/\tilde{\sigma})^2}}, \quad \text{with} \quad f_0 = \frac{C_R}{C_R-1} \tag{2.17}$$

Here, σ is a local shear parameter defined as $\sigma = (k/\varepsilon)\sqrt{(\partial U_i/\partial x_j)^2}$, and $\tilde{\sigma}$ is its corresponding value in an idealised neutral logarithmic surface layer. The model constant C_R is calibrated to 4.5 based on LES comparisons. By construction, $f_P = 1$ in neutral log-law conditions, and $f_P < 1$ in regions where $\sigma > \tilde{\sigma}$.

The eddy viscosity expression is thus modified to:

$$\nu_T = C_\mu f_P \frac{k^2}{\varepsilon} \tag{2.18}$$

Originally calibrated using LES of single-turbine wakes, the model has shown improved predictions of wake deficits in aligned rows under low ambient turbulence conditions [37]. In complex terrain, the same mechanism could help suppress over-diffusion in shear-dominated flow regions and delay recovery after terrain-induced separation, consistent with the physical suppression of mixing expected in stably stratified or recirculating zones.

2.2.4 *The* k-ε-MO(B) *Turbulence Model*

The k-ε-MO model builds upon the standard k-ε turbulence model by incorporating stability effects via Monin-Obukhov Similarity Theory [34]. This allows the model to simulate non-neutral atmospheric surface layers, capturing variations such as stable and unstable conditions. In PyWakeEllipSys, the stability parameter ζ, introduced in Section 2.1 as $\zeta = z/L$, the roughness length z_0 is numerically added to z to account for surface roughness [36]:

$$\zeta = \frac{z+z_0}{L}, \tag{2.19}$$

where L is the Obukhov length, which adjusts for the effects of buoyancy. For neutral conditions, $\zeta = 0$, reducing the model to the standard k-ε setup. In non-neutral conditions, ζ influences the inflow velocity, turbulent kinetic energy (k), and dissipation rate (ε), enabling a more realistic representation of stratified flows.

The inflow velocity and turbulence parameters are set based on reference turbulence intensity (TI_{ref}) and stability at a specified height (z_{ref}). For complex terrain, the roughness length (z_0) is a characteristic of the terrain which is known from the site analysis. Therefore, TI_{ref} can be set such that the roughness length remains a chosen constant:

$$TI_{ref} = \frac{\kappa \sqrt{\frac{2}{3}\left(\frac{\phi_\varepsilon(\zeta_{ref})}{C_\mu \phi_m(\zeta_{ref})}\right)^{1/2}}}{\ln\left(\frac{z_{ref}+z_0}{z_0}\right) - \Psi_m(\zeta_{ref})}, \tag{2.20}$$

where the dimensionless stability functions for momentum and dissipation rate are defined as follows:

$$\phi_m(\zeta) = \begin{cases} (1-\gamma_1\zeta)^{-1/4}, & \text{for } \zeta < 0 \\ 1+\beta\zeta, & \text{for } \zeta \geqslant 0 \end{cases} \tag{2.21}$$

$$\phi_\varepsilon(\zeta) = \begin{cases} 1-\zeta, & \text{for } \zeta < 0 \\ 1+(\beta-1)\zeta, & \text{for } \zeta \geqslant 0 \end{cases} \tag{2.22}$$

$$\Psi_m(\zeta) = \begin{cases} \ln\left(\frac{1+x^2}{2}\right) + \ln\left(\frac{1+x}{2}\right)^2 - 2\arctan(x) + \frac{\pi}{2}, & \text{for } \zeta < 0, \quad x = (1-\gamma_1\zeta)^{-1/4} \\ -\beta\zeta, & \text{for } \zeta \geqslant 0 \end{cases} \tag{2.23}$$

These functions adjust the wind shear and logarithmic wind profile based on atmospheric stability, essential for accurate modelling under non-neutral conditions [3, 33].

The k-ε-MO turbulence models transport equations both include a source/sink term B for buoyancy, which is based on MOST. While the k-ε-MOB model is a modified version of the k-ε-MO approach, where this term is constant, defined as:

$$B = -\frac{u_*^3}{\kappa L}, \tag{2.24}$$

where u_* denotes the friction velocity, κ is the von Kármán constant, and L is the Obukhov length. This modification removes the dependency on the local velocity gradients, which can cause non-physical results of wake recovery trends [36] under unstable conditions.

3

PERDIGÃO SITE DESCRIPTION & DATA HANDLING

In this chapter, the Perdigão measurement campaign is introduced, and context of the site chosen for this study is provided. First, the geographical setting and terrain characteristics are outlined, followed by an overview of the instrumentation and data collection methods. Finally, the prevailing meteorological conditions, including wind climate and stability patterns, are described.

3.1 SITE SELECTION

The primary goal of site selection is to illustrate the challenges involved in estimating wind resources on a terrain typified by features like steep slopes and flow separation, focusing particularly on flows reaching the heights typical of modern large wind turbines (over 100 meters above ground level). The aim was to create a moderately complex setting that builds on the foundation of the Askervein Hill research [57] and similar microscale studies. Along with core wind-energy parameters such as wind speed and turbulence profiles, the campaign intended to assess spatiotemporal gradients and turbulent fluxes impacting atmospheric boundary layer stability [19]. This requires at least one primary mast for reference and one or more additional masts distributed across topographic features. Multiple field studies were evaluated for this purpose, including Bolund Hill [6], Askervein Hill [57], Perdigão Mountain [42], and the Alaiz region [10].

For this study, Perdigão Mountain was selected. Perdigão Mountain in Portugal is the largest of the New European Wind Atlas (NEWA) campaigns, which hosted an extensive field campaign in 2017. Major deciding factors were the quasi-2D doubleparallel-ridge topography, approximate ridge-normal annual wind climatology and horizontally isotropic turbulence [19].

3.2 LOCATION, TOPOGRAPHY AND LAND COVER CHARACTERISTICS

The Perdigão experimental site is situated in central Portugal, within the Vale do Cobrão near the town of Perdigão, located northeast of Porto. The site is characterized by a unique topographical formation consisting of two nearly parallel ridges, creating a quasi-two-dimensional valley.

Spatial data related to the Perdigão experimental site are referenced using the Universal Transverse Mercator (UTM) coordinate system. Specifically, coordinates have been reprojected into the UTM Zone 29N, which is based on the WGS84 datum. Coordinates within this system are represented in meters east (Easting) and meters north (Northing) from a defined origin.

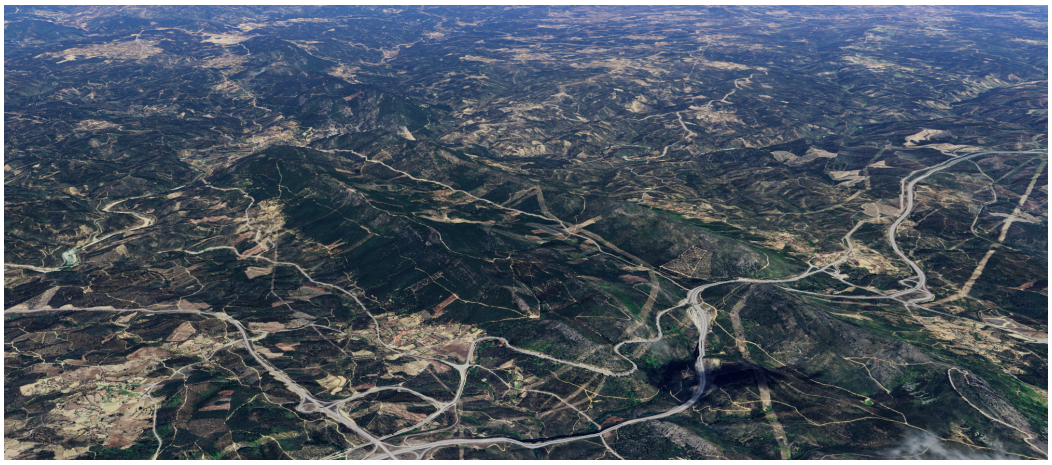

Figure 3.1: Satellite view of Perdigão Site (Google Earth)

The main ridges are separated by a narrow valley of about 1.5 km wide, running parallel along approximately 4 km in length. Elevations in the area range from approximately 150 m at the valley floor to over 500 m at the ridge tops. The ruggedness of the Perdigão terrain has been quantified using the Ruggedness Index (RIX) as introduced in Section 2.1. The RIX values for the southern ridge, valley, and northern ridge at the Perdigão site are approximately 14.6 %, 13.5 %, and 14.0 %, respectively. RIX values above 10 % are often considered indicative of significantly complex terrain in the context of linearised flow models, where terrain-induced speed-up and flow separation effects may not be reliably captured [5].

The contour elevation map presented in Figure 3.2 was generated from high-resolution raster data using Python-based `Windkit` and `PyWAsP` using the NASA Digital Elevation Model (NASADEM), providing an accurate portrayal of the ridge lines, valley floors, and transitional slopes that shape the site's wind conditions. Some mast locations of interest are also indicated in Figure 3.2 and will be further discussed in the experimental setup description. Additionally, the single 2 MW wind turbine present on the southern ridge is marked approximately 300 m north-west of the western ridge top mast.
Surface characteristics around the Perdigão experimental site were derived from high-resolution raster-based land-cover maps, exemplified in the right panel of Figure 3.3. These raster products, sourced from ESA's Climate Change Initiative (CCI) [17], capture spatial distributions of vegetation and anthropogenic surfaces, which significantly influence roughness length z_0 and displacement height d. The roughness lengths corresponding to their respective land-cover IDs are summarised in Appendix A.1. The roughness patterns primarily consist of dense tree cover located on ridge tops, contributing to increased roughness lengths ($z_0 > 1.0$ m), whereas agricultural and bare land areas in the valley exhibit much lower roughness values ($z_0 < 0.1$ m).

3.3 EXPERIMENTAL LAYOUT AND MEASUREMENT CAMPAIGN

The Perdigão site was equipped with extensive instrumentation to capture wind conditions across its complex terrain, with measurements performed during an intensive observational

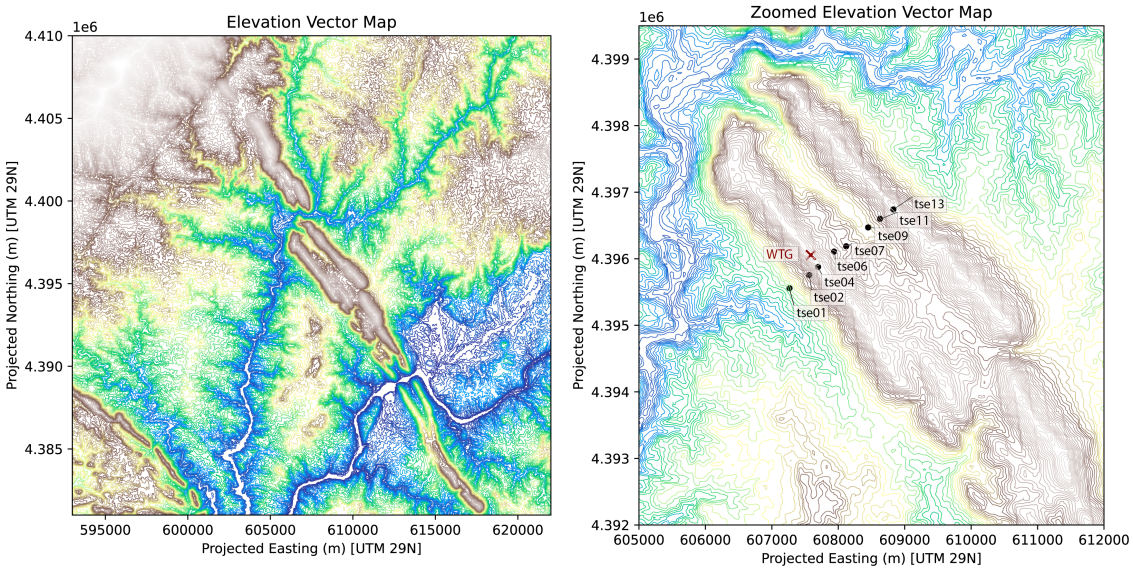

Figure 3.2: Elevation Contour Map. Meteorological masts are denoted by 'tse'.

period (IOP) in 2017. While dual-lidar scanning data was collected simultaneously to complement mast measurements, the current study restricts analysis to meteorological mast data. Lidar data is not included due to its inherent complexity, higher uncertainty during complex flow conditions, and the added complexity in data processing, which would not align with the primary validation scope of the current investigation, focusing explicitly on mast-measured data.

3.3.1 *Meteorological Masts*

Among the available instrumentation, a reference mast (tse01) equipped with CSAT3A sonic anemometers up to 30 m a.g.l, and three additional meteorological masts (tse04, tse09, and tse13) equipped with Gill WM Pro 3-axis sonic anemometers and air temperature/humidity meters up to 100 m a.g.l are of primary interest. These masts were strategically placed to represent different topographic features, allowing investigation of spatial gradients and vertical wind profiles relevant to wind resource assessment validation studies. The exact positions and elevations of these masts are detailed in Table 3.1.

Table 3.1: Meteorological masts at Perdigão: UTM 29N projected coordinates and elevations.

Mast	Easting (m)	Northing (m)	Elevation (m)
tse01	607266.2	4395556.6	255.8
tse04	607696.0	4395877.6	473.0
tse09	608449.3	4396470.3	305.3
tse13	608829.6	4396740.7	452.9

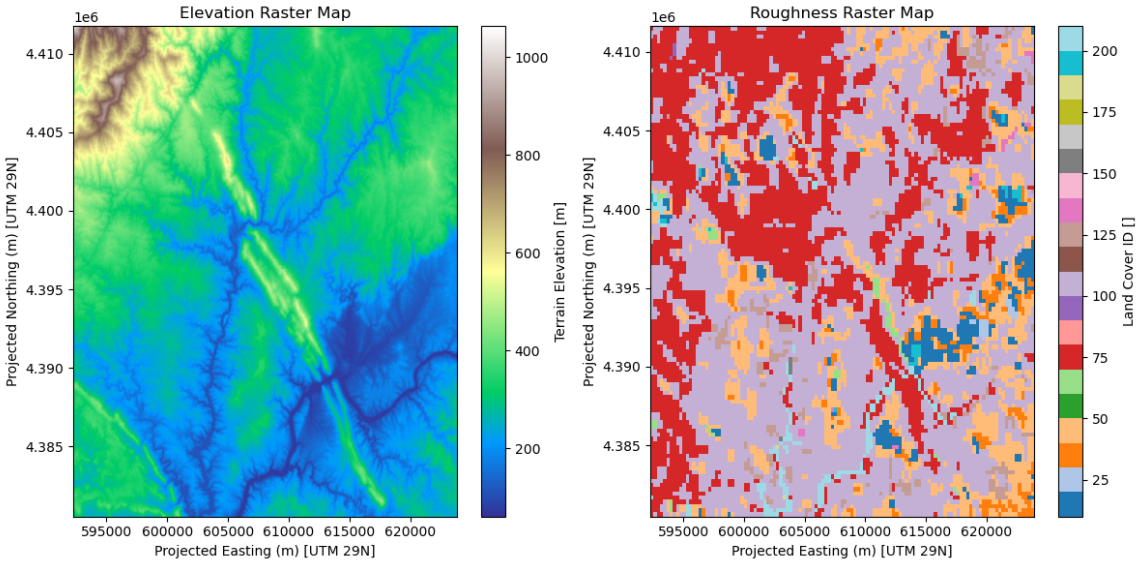

Figure 3.3: Elevation and Roughness Raster Maps

A detailed overview of the selected meteorological masts is presented in Table 3.2 and Figure 3.4. Temperature sensors allow for the evaluation of the stability of the Atmospheric Surface Layer (ASL), which is further discussed in Section 3.4.

Table 3.2: Measurement heights a.g.l. (m) for sonic anemometers and temperature sensors at selected masts.

Mast	**Sonic Anemometer Heights a.g.l (m)**	**Temperature Sensor Heights a.g.l (m)**
tse01	9.91, 28.79	–
tse04	10, 20, 30, 40, 60, 78, 100	2, 10, 100
tse09	10.38, 20.51, 30.14, 40.6, 60.15, 80.28, 97.47	2, 10, 100
tse13	10.02, 20.02, 30.12, 40.03, 60.15, 79.97, 97.04	2, 10, 100

The orientation of sonic anemometers was carefully selected to minimise flow distortion, with measurement booms typically oriented parallel to local height contours and pointing predominantly up-valley (approximately south-east). Precise azimuth, pitch, roll, and height measurements were performed using DTU's multistation to correct tilt and accurately report wind data in geographic coordinates [42].

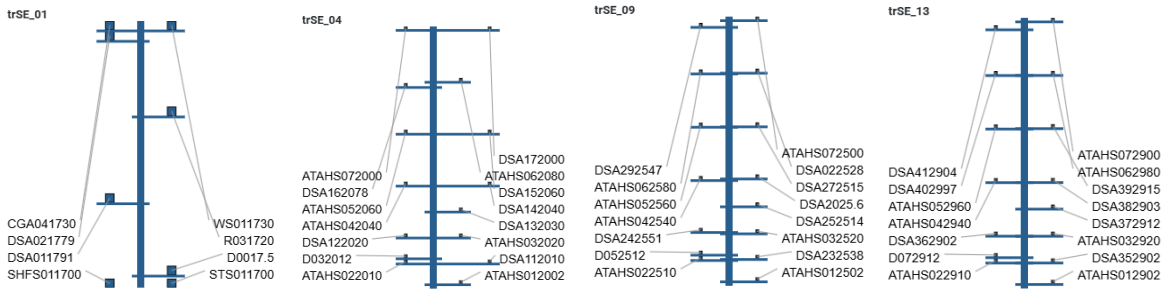

(a) tse01 (b) tse04 (c) tse09 (d) tse13

Figure 3.4: Vertical layouts and sensor configurations of selected Perdigão meteorological masts. Heights and sensor types correspond to those listed in Table 3.2 [42].

3.3.2 *Data Management and Availability*

Data availability varied over the course of the Perdigão campaign due to sensor outages, maintenance operations, and weather-induced interruptions. For this reason, a specific intensive observation period (IOP) from 26 April to 17 June 2017 was selected for further analysis. This period was characterised by continuous and simultaneous operation of all required instrumentation, including sonic anemometers and temperature sensors on the three selected towers. Figure 3.5 visualises the overall data coverage and highlights the selected IOP.

As a first filtering step, only time intervals within this IOP were retained, reducing the dataset from 20736 to 14976 five-minute samples. In addition, any samples containing missing values (NaNs) in the relevant channels across the three towers were excluded. This ensured that all remaining time intervals used for the analysis contain valid, synchronised data from all sensors. The subsequent filtering steps are introduced in Section 3.5, and the number of samples retained at each stage is summarised in Table 3.3.

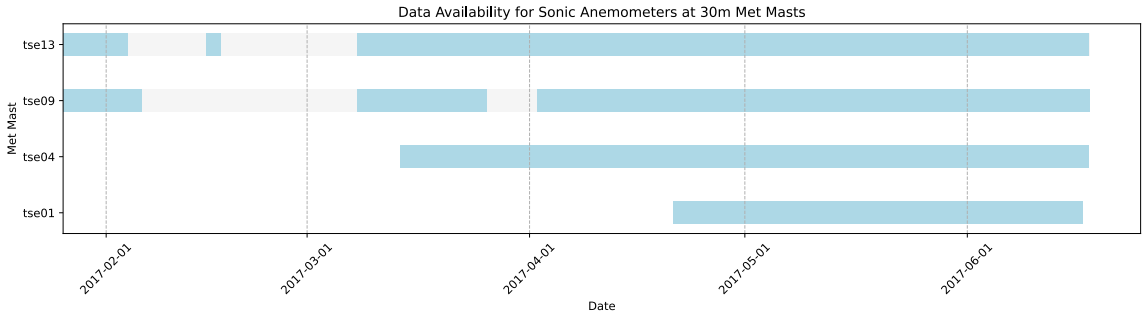

Figure 3.5: Availability of measurement data from towers tse01, tse04, tse09, and tse13.

The utilised dataset comprises quality-controlled, tilt-corrected 5-minute averages of high-frequency data measurements from all instruments deployed during the campaign. Data subsets relevant to this analysis were retrieved through the OpenPDAP interface, using a custom-developed Python script to access and process data subsets programmatically.

3.4 WIND CLIMATE

The Perdigão site exhibits a wind climate strongly shaped by its distinctive topography, characterised by two quasi-parallel ridges bounding a narrow valley. Early observations by Fernando et al. (2019) highlighted a prevailing synoptic-scale wind direction roughly normal to the ridges [19], yet local deviations from this pattern arise from orographic interactions typical of steep terrain. In particular, flow channelling occurs when horizontal winds follow the path of the valley due to pressure differentials induced by the terrain's shape, while slope acceleration results from air being forced over elevated contours. Such processes are well-documented in boundary-layer and mountain meteorology, where synoptic forcing, local thermally driven circulations, and topographic constraints can substantially modify near-surface wind fields [32].

During the intensive observational period, wind-rose diagrams were generated at a 100 m measurement height for masts tse04, tse09, and tse13, as shown in Figure 3.6. Analysing these plots reveals differences in the prevailing wind directions, which reflect each mast's position relative to topographic features. At the valley-floor mast (tse09), winds often align with the valley axis, indicative of strong channelling effects within the confined corridor between the two ridges. In contrast, the ridge-top masts (tse04 and tse13) experience winds oriented largely perpendicular to the valley, consistent with the broader synoptic flow impinging on the ridges and accelerating over the elevated terrain. These ridge-top flows frequently attain moderate to high wind speeds due to terrain-induced speed-up mechanisms, which are widely reported in regional wind-energy assessments and mountain meteorology studies [58].

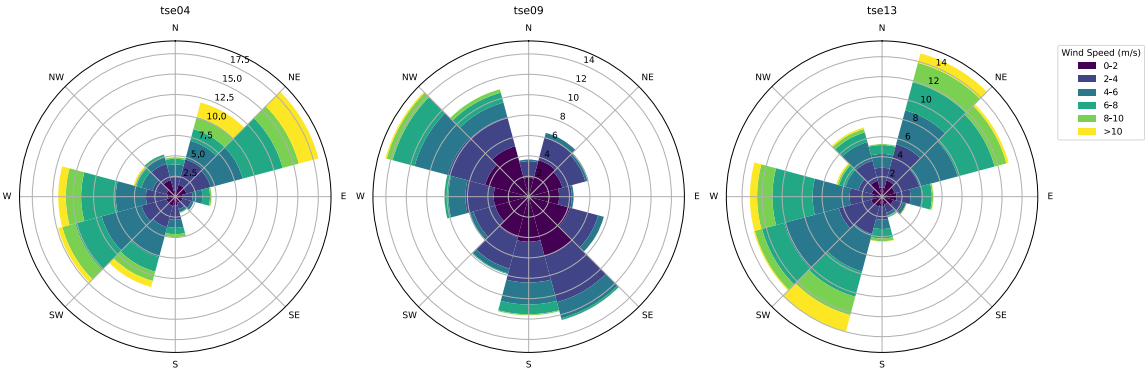

Figure 3.6: Wind Rose from 100m masts

Overall, the Perdigão wind regime reflects a balance among large-scale weather patterns, local orographic forcing, and thermal circulations. As documented by Fernando et al. (2019) [19], local terrain effects can substantially modify ridge-normal synoptic flows, leading to pronounced variability in wind speed and direction across short spatial scales. Two major mesoscale flow regimes dominate in complex terrains such as Perdigão: thermal circulation driven by topographic heating and cooling, and synoptically forced flows interacting with the topography (see Figure 3.7).

Thermal circulation includes anabatic (upslope) flows from surface heating and katabatic (downslope) flows due to nocturnal radiative cooling and buoyancy-driven cold-air drainage [59]. Katabatic flows can lead to stable stratification and cold-air pooling if outflow is restricted, creating complex internal dynamics [20]. During daytime, upslope convection and valley subsidence can induce deep convection [2]. Transition periods around sunset and sunrise involve rapid slope wind reversals, producing flow separation and complex interactions [28].

Synoptically driven flows dominate when larger-scale atmospheric motions interact with terrain features, influencing flow structure primarily through stratification effects. In neutrally stratified flows, modest slopes induce flow acceleration, while steep slopes can lead to separation, recirculation, and coherent vortical structures [31]. Under stable stratification, multiple phenomena including lee waves, internal waves, rotors, hydraulic jumps, recirculation zones, shear layers, and upstream blocking may develop [1]. At Perdigão, parallel ridges significantly enhance these phenomena through dynamic interactions between separated flows and valley circulations [15, 49].

Some flow processes studied by Perdigão investigators are summarised in Figure 3.7. Additionally, topographic gaps along ridge lines further increase complexity, particularly under stable stratification conditions, resulting in phenomena like hydraulic jumps and gravity wave breaking [13, 22].

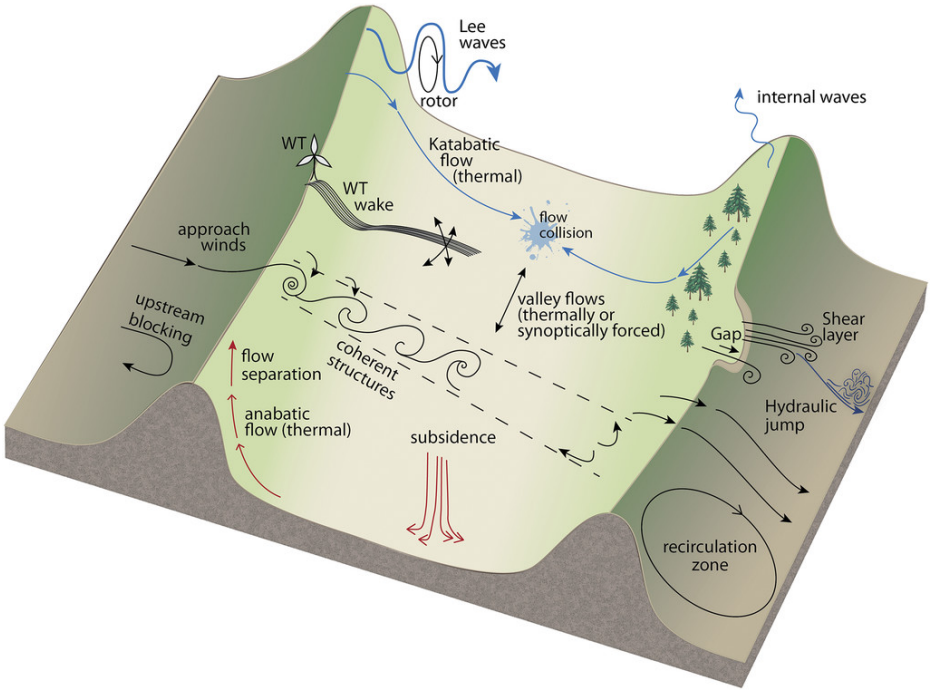

Figure 3.7: Possible microscale processes in an idealized 2D valley [19].

3.4.1 *Stability Analysis*

Characterising atmospheric stability in complex terrain remains challenging due to significant topographic forcing, diurnal heating variations, and local flow modifications [54, 60]. In this study, atmospheric stability is assessed using the Monin-Obukhov similarity theory, introduced in Section 2.1 [21, 46].

Stability calculations utilise data from mast tse09, selected due to its representative location within the valley. MOST, assuming horizontally homogeneous terrain and a steady, planar flow field, is likely more valid here than on the hill tops, where flow is typically distorted by strong terrain-induced accelerations, pressure gradients, and increased turbulence due to separation and curvature effects. Furthermore, this mast is equipped with high-quality ultrasonic anemometers and temperature sensors. Measurements at a height of 10 m were chosen to minimise influence from local surface roughness elements while remaining within the atmospheric surface layer, ensuring compatibility with MOST assumptions [21, 54].

The Obukhov length (L) is defined by

$$L = -\frac{u_*^3 \bar{\theta}}{\kappa g \overline{w'\theta'}}, \tag{3.1}$$

where u_* is the friction velocity, $\bar{\theta}$ is the mean potential temperature, $\overline{w'\theta'}$ is the vertical kinematic turbulent heat flux, $\kappa \approx 0.4$ is the von Kármán constant, and g is gravitational acceleration. The friction velocity is derived from measured turbulent momentum fluxes:

$$u_* = \left(\overline{u'w'}^2 + \overline{v'w'}^2\right)^{1/4}, \tag{3.2}$$

where $\overline{u'w'}$ and $\overline{v'w'}$ are the horizontal turbulent momentum fluxes [54].
The mean potential temperature ($\bar{\theta}_z$) at measurement height z is obtained from air temperature measurements corrected by the dry adiabatic lapse rate ($\Gamma = 0.0098$ K m^{-1}): In this analysis, relatively dry conditions are presumed due to limited barometric data. Nevertheless, consistency checks indicate that temperature offsets among the 100-m towers remain modest (below 3.8 K), lending support to this assumption [14].

$$\bar{\theta}_z = T_z + \Gamma \cdot z. \tag{3.3}$$

The vertical kinematic turbulent heat flux ($\overline{w'\theta'}$) is derived from measured temperature flux ($\overline{w'T'}$) using the conversion:

$$\overline{w'\theta'} = \overline{w'T'}\left(1 + \frac{\Gamma z}{T_z}\right). \tag{3.4}$$

As introduced in Equation 2.19 in Section 2.2, the stability parameter (ζ) is defined as the ratio of the measurement height (z) plus the surface roughness (z_0) to the Obukhov length (L). A surface roughness length z_0 of 0.8 m was chosen from the Roughness Raster Map (Figure 3.3) converted using Table A.1 found in Appendix A.1.

The stability classes previously defined in Table 2.1 of Section 2.1 were used to classify each 5-minute average data point to its respective stability condition. Furthermore, wind speeds below 7 m s^{-1} are excluded to avoid instability in the determination of turbulent fluxes under weak wind conditions [54].

Figure 3.8 shows the diurnal cycle of ζ at mast tse04, illustrating a common pattern of stable conditions during nighttime and unstable conditions during daytime due to solar heating and convective mixing. Unstable conditions are shown to peak in the afternoon, and stable conditions prevail at night. Such diurnally driven stability shifts are well-documented in mountainous regions, where solar heating of slopes and valley floors strongly modulates buoyancy and turbulence [54, 60].

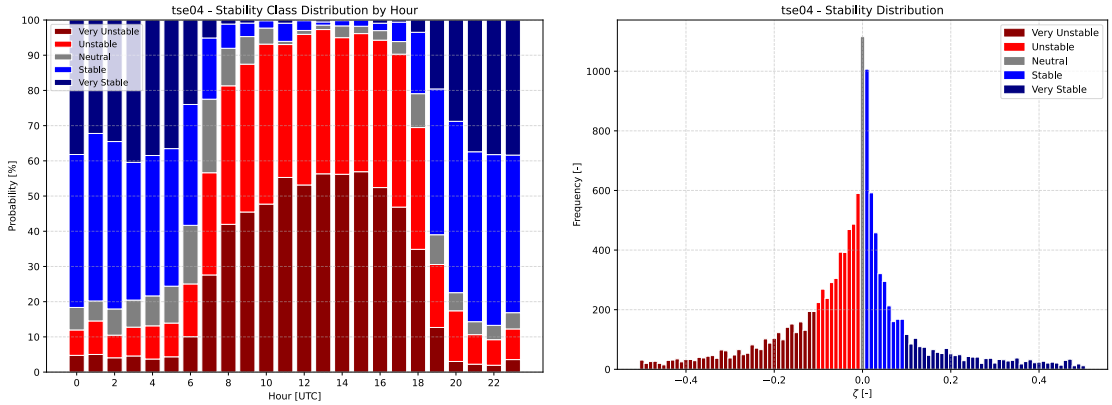

Figure 3.8: Hourly distribution (left) and histogram (right) of stability cases at tse04 (before filtering).

Despite these general patterns, the hourly stability distribution reveals deviations that highlight the limitations of MOST in complex terrain. For example, Figure 3.8 shows occurrences of strongly unstable conditions persisting well into the night, as well as stable conditions appearing sporadically throughout the day. These features suggest that the local stratification near the surface may not always align with the broader thermal or dynamical forcing. Additionally, while neutral conditions are most frequent near sunrise and sunset, neutral stratification is present across nearly all hours. This behaviour reflects the spatial heterogeneity of surface fluxes, slope exposures, and wind shear in mountainous regions—conditions under which the assumptions used in MOST break down [26, 44].

3.5 MEASURED PROFILE SELECTION

The final objective of the data handling process is to derive a consistent set of validation profiles that can be directly compared to the simulation results. This involves computing vertical profiles of wind speed and wind direction for each stability class, applying appropriate filtering criteria, and addressing directional ambiguities arising from terrain-induced variability in the valley mast.

Each stability class is treated separately using a consistent three-stage filtering approach: (1) temporal selection based on the IOP, (2) minimum wind speed filtering to remove low-wind

artefacts, and (3) wind direction filtering centred around the inflow direction which in this case is set to $240° \pm 10°$, applied at the ridge-top mast tse04 at 100 m. The corresponding filtering parameters and masks are defined in `Data_handling.py` and applied uniformly across all towers and heights to ensure comparability. Only time points satisfying all three filters and classified within a given stability regime are retained.

Table 3.3: Number of 5-minute samples retained after each filtering step, including distribution by stability class.

Filtering Step	**Remaining Samples**
Initial dataset	20736
After IOP filter (26 Apr – 17 Jun 2017)	14976
After wind speed filter ($U > 7.0$ m/s at tse04 100 m)	3499
After wind direction filter ($240° \pm 10°$ at tse04 100 m)	315
Neutral	91
Stable	91
Unstable	132

For each filtered subset, vertical profiles of wind speed and wind direction are constructed using the masts tse01 (reference), tse04 (upwind ridge), tse09 (valley), and tse13 (downwind ridge). Speed-up values are computed by normalising wind speeds at each height by the mean wind speed at the reference mast tse01 at 30 m. The standard error of the mean (SEM) is used to indicate how different the population mean is likely to be from a sample mean and is computed as:

$$\mathrm{SEM} = \frac{\sigma}{\sqrt{n}}, \tag{3.5}$$

where σ is the sample standard deviation and n is the number of samples included in the filtered subset. Examples of the resulting profiles are presented in Figure 3.9 and Figure 3.10.

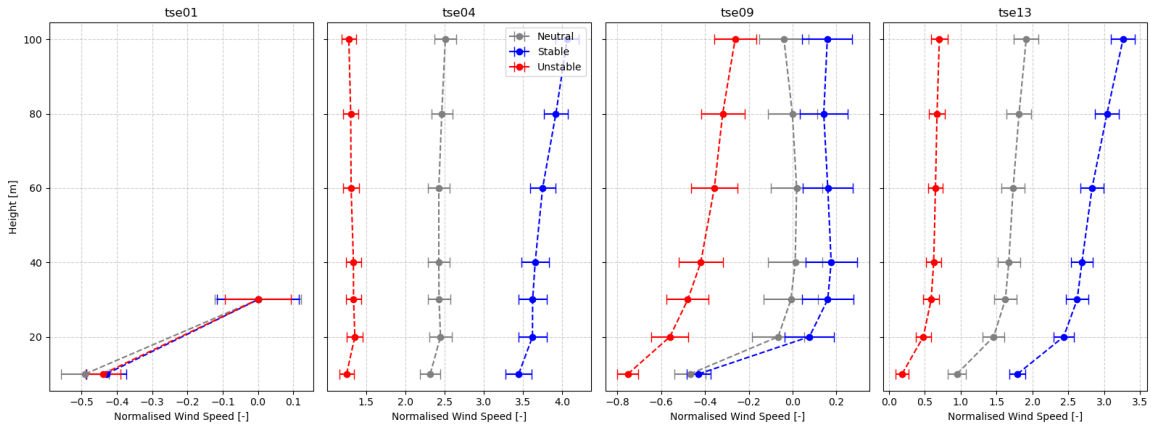

Figure 3.9: Measured vertical profiles of normalised wind speed (speed-up).

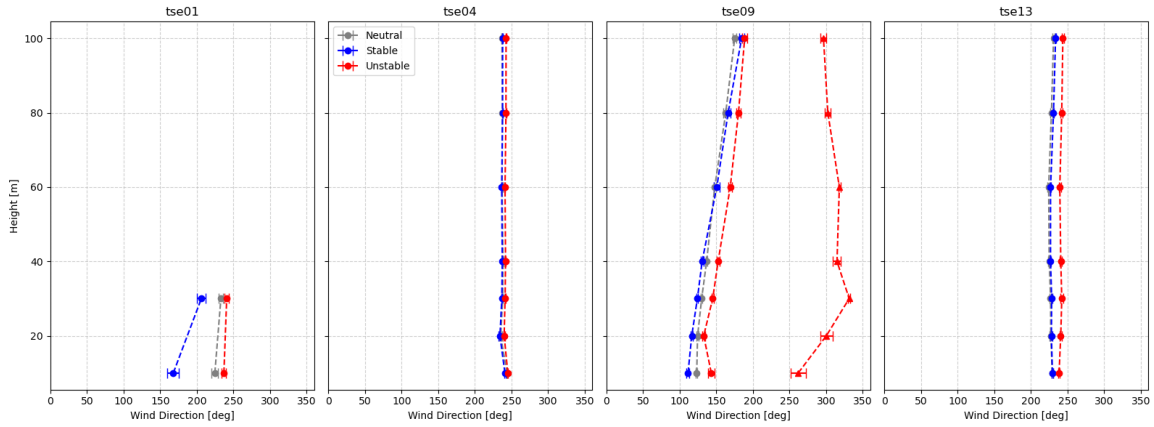

Figure 3.10: Measured vertical profiles of wind direction.

Special attention is given to the valley mast tse09, where the wind direction data under unstable conditions exhibits a pronounced bimodal structure, as shown in Figure 3.11. This behaviour could be explained by the dynamic interaction of thermally and synoptically driven flows in the confined valley geometry, resulting in time-dependent directional shifts that cannot be captured by simple filtering alone. If one were to compute average wind directions from such a dataset without resolving the individual modes, the resulting mean would lie somewhere between the two dominant directions. This is not physically meaningful in the context of flow structure, as such a mean direction does not represent any actual flow state that occurred.

This is handled by identifying peaks using the `scipy.signal.find_peaks` method, with a prominence threshold set to 20% of the maximum bin count to filter out spurious or low-contrast modes. This ensures that only statistically relevant modes are extracted. Once peak locations are determined, each wind direction sample is assigned to its nearest mode within a 30° window.

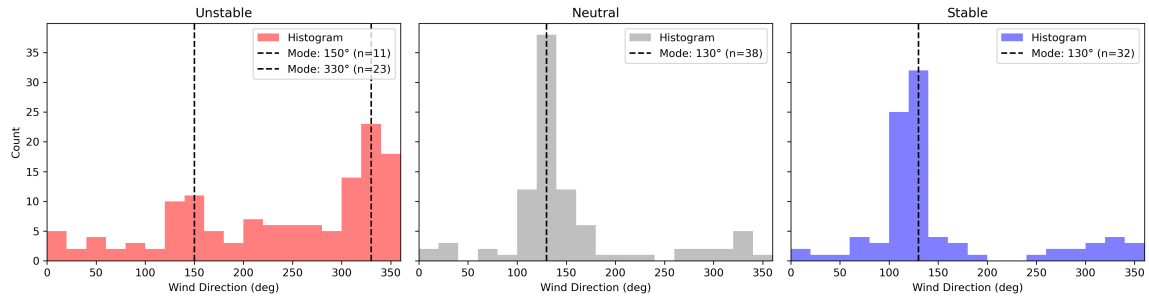

Figure 3.11: Histogram of wind direction at tse09 at 30 m, classified by stability regime.

TI profiles are extracted from the same filtered measurement subsets described in Section 2.1. As introduced in Section 2.1.4, TI is defined as the ratio of velocity fluctuations to the local mean wind speed. However, using this definition directly in validation introduces an additional source of uncertainty, since both k and U are modelled quantities. To isolate model performance in predicting turbulent kinetic energy, TI is instead normalised using a single reference wind speed measured at the reference tower.

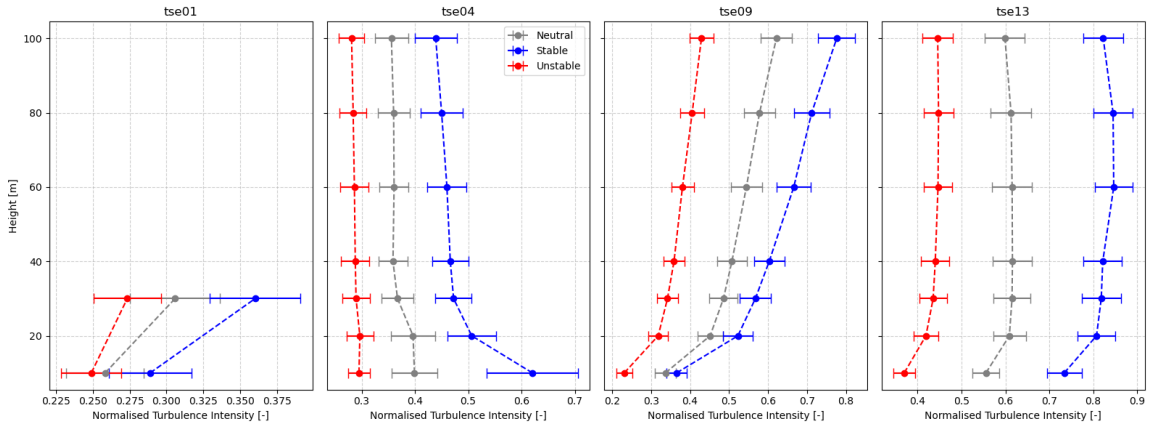

Figure 3.12: Measured vertical profiles of normalised TI.

This final dataset provides a stability-conditioned, directionally consistent benchmark for validating the RANS simulations under characterised inflow conditions for stable, neutral and unstable conditions. Each stability class is associated with a separate simulation that aims to reproduce the representative inflow conditions observed in the field campaign as closely as possible. For this purpose, mean values of friction velocity, Obukhov stability parameter, and TI are computed for each class using the filtered subset of data described above. Including the TI correction following from the isotropic turbulence assumption described in Section 2.1.4.

Table 3.4: Mean inflow parameters derived from filtered data used to define simulation inflow conditions.

Stability Class	**Friction Velocity u_* (m s^{-1})**	**Stability Parameter ζ**	**TI**
Neutral	0.515 ± 0.018	0.000 ± 0.001	0.140 ± 0.011
Stable	0.328 ± 0.016	0.250 ± 0.071	0.101 ± 0.005
Unstable	0.438 ± 0.015	-0.420 ± 0.109	0.133 ± 0.003

These mean values will be used to define the inflow boundary conditions in the RANS simulations for each stability regime. While the simulations are not designed to reproduce each measurement, the use of averaged and stability-specific inflow parameters ensures that the numerical cases are representative of the filtered observational subsets used for validation.

4

METHODOLOGY

PyWakeEllipSys is a Reynolds-averaged Navier-Stokes (RANS)-based extension to the PyWake wind farm modelling library, developed at DTU by van der Laan et al. (2024) [36]. It integrates with the EllipSys3D solver through PyEllipSys, a Python interface that enables programmatic simulation control. EllipSys3D, originally developed by Michelsen [45] and further extended by Sørensen [55], provides the finite-volume flow solver and associated preprocessing tools. The structure of this toolchain is shown in Figure 4.1.

This modular coupling allows users to simulate atmospheric boundary layer flows over flat and complex terrain using a RANS approach. Although PyWakeEllipSys supports turbine wake modelling, the present study focuses on terrain effects and inflow validation, where the solver's capability to handle topographic detail is central to wind resource assessment.

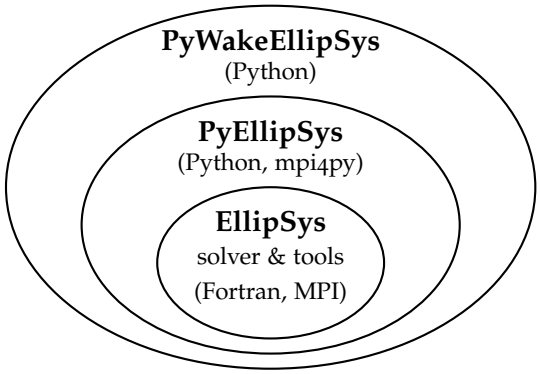

Figure 4.1: Component structure of the PyWakeEllipSys framework.

4.1 COMPUTATIONAL GRID GENERATION

The computational mesh used in this study is generated using `PyWakeEllipSys`, employing a structured O-grid topology optimised for terrain-resolving RANS simulations [38]. The `terrainogrid` configuration provides a body-fitted structured grid that accommodates steep slopes, smooths farfield features, and maintains computational stability during iterative solution of the flow equations.

Elevation and roughness data are imported from WAsP-formatted contour maps and converted internally to `.grd` format using `grid_terrain_map`. These terrain inputs, introduced in Chapter 3, provide the required surface characteristics for setting both the inner and outer domain layers. The mesh consists of two regions: a high-resolution inner domain, set to 2.4 km centred on the tse09 mast, and an outer domain spanning 42.5 km that buffers terrain transitions towards the farfield. The complete parameter set used for the grid generation is summarised in Table 4.1, largely based on the practice in Das (2021) for complex terrain convergence studies [16].

Table 4.1: Summary of terrain grid configuration for Perdigão simulations.

Grid Parameter	**Symbol / Keyword**	**Value**
Grid type	`type`	`terrainogrid`
Domain centre	`origin`	Coordinates of tse09 mast
Reference rotor diameter	D	120 m
O-grid radius	`radius_D`	750D
Domain height	`zlen_D`	25D
Inner margin size	`m1_x_D`	20D in all directions
Inner grid resolution	`cells1_D`	8.0
Outer domain width	`terrain_map_Lxy_outer`	42500 m
Outer grid resolution	`terrain_map_dxy_outer`	25 m
First cell height	`zFirstCell_D`	0.0005D
Vertical stretching profile	`zdistr`	`waspcfd75`
Vertical resolution end (wake region)	`zWakeEnd_D`	10.0
Block edge discretisation	`bsize`	48
Wind direction sectors	`dwd`	360°
Farfield height mode	`terrain_map_farfield_h`	−1 (terrain-following)
Farfield roughness	`terrain_map_farfield_z0`	0.8 m
Terrain smoothing	`terrain_map_smooth`	Enabled
Radial smoothing start	`terrain_map_smooth_rmax`	20000 m
Surface grid generator	`terrain_surfgen`	`hypgridsf`
3D hyperbolic blend factor	`terrain_hyp3d_blendf`	0.05/`cells1_D`
Surface blending factor	`terrain_hypsf_blendf`	0.05/`cells1_D`
Outer cell radial spacing control	`terrain_ogrid_dr`	−1 (auto-expanding)

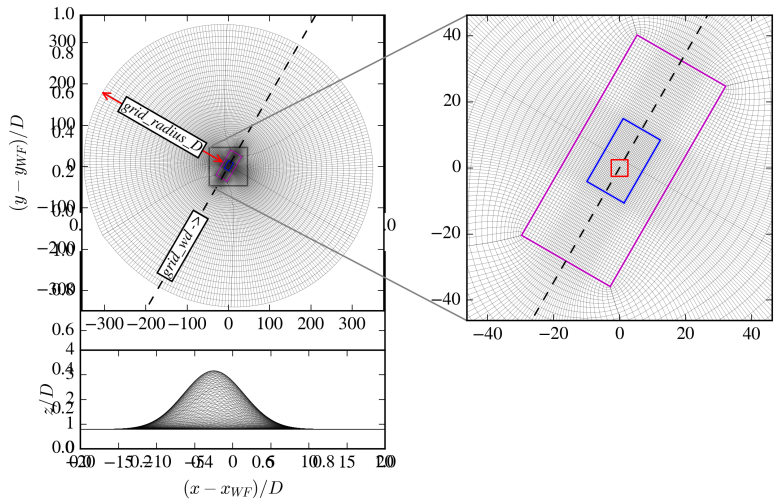

Figure 4.2: Surface O-grid topology constructed using `terrainogrid` for idealised terrain [38].

To suppress boundary effects, radial terrain smoothing is applied to the outer domain. This process blends the original terrain elevation $h(\theta, r)$ with a reference farfield height $h_{\text{farfield}}(\theta)$, using the transition function defined in Equation 4.1, adapted from PyWakeEllipSys documentation [38]:

$$h_{\text{smooth}}(\theta, r) = h(\theta, r) + \tanh\left[\operatorname{atanh}(0.99)\left(\frac{r - r_{\min}}{0.99 r_{\max} - r_{\min}}\right)^{c}\right](h(\theta, r) - h_{\text{farfield}}(\theta)), \quad (4.1)$$

where $h(\theta, r)$ is the original terrain elevation at polar coordinates (θ, r), h_{smooth} is the smoothed terrain, and $h_{\text{farfield}}(\theta)$ is the farfield reference height for direction θ. The smoothing acts radially from a minimum radius $r_{\min}$ to a maximum domain radius $r_{\max}$, with the sharpness of the transition controlled by the exponent c.

The farfield height $h_{\text{farfield}}(\theta)$ is computed per wind direction using exponentially weighted radial averaging, as defined in Equation 4.2:

$$h_{\text{farfield}}(\theta) = \frac{\int_{r_{\min}}^{L_{xy}/2} h_{\text{smooth}}(\theta, r) \exp\left(-\frac{r - r_{\min}}{10^4}\right) dr}{\int_{r_{\min}}^{L_{xy}/2} \exp\left(-\frac{r - r_{\min}}{10^4}\right) dr} \quad (4.2)$$

where L_{xy} is the horizontal domain width and the exponential decay factor controls the weighting distance.

The vertical grid is defined using a tanh-based stretching function, starting from a minimum cell height of 0.0005D at the surface and extending up to 25D, where D is the rotor diameter. The `waspcfd75` option allocates 75% of the vertical grid points within the first 1000 m above the terrain, enhancing near-surface resolution.

The domain employs a single grid across all wind directions (`dwd` $= 360°$), avoiding directional grid artefacts. Boundary conditions are automatically assigned as mixed inlet/outlet on lateral sides, while the bottom boundary resolves the terrain surface with spatially distributed roughness length (z_0) derived from raster data.

The resulting domain configuration is shown in Figure 4.3. Inner, outer, and wake domains are highlighted. The roughness length distribution applied to the surface mesh is shown in Figure 4.4.

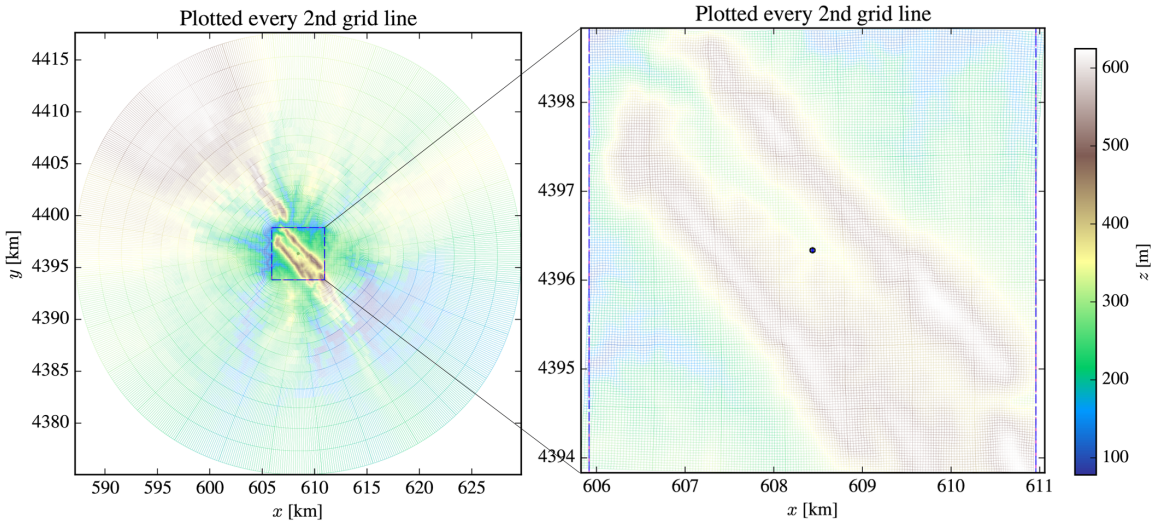

Figure 4.3: Full terrain O-grid generated by PyWakeEllipSys.

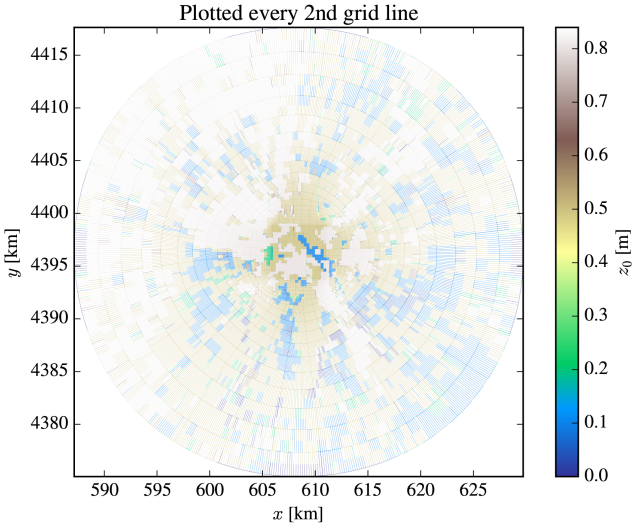

Figure 4.4: Surface roughness length (z_0) map for the computational domain.

4.2 SIMULATION METHODOLOGY

Following the grid generation described in Section 4.1, each simulation case is executed for a representative set of wind directions and turbulence models, allowing a systematic evaluation of model behaviour across different flow regimes.

All simulations are performed on a fixed terrain-resolved grid, using five wind directions spaced at 5° intervals between 230° and 250°, centred around 240°

Each case is simulated independently using one of four turbulence closures: the standard k–ε model (`ke`), its length scale limited variant (`kefp`), and the Monin–Obukhov

based versions (`keMOB` and `keMOBfp`) for stable and unstable stratification (as introduced in Section 2.2.

4.2.1 *Boundary Conditions*

The lower boundary of the 3D domain is modelled as a rough wall, using the wall-function formulation described by Sørensen (2007) [56]. This method is designed to accommodate flexible placement of the first computational cell above ground without enforcing a strict vertical resolution. Rather than prescribing a velocity at the surface, the wall shear stress τ_w is computed implicitly as

$$\tau_w = \rho \left[\frac{\kappa U(z_P)}{\ln\left(1 + \frac{\Delta z}{z_0}\right)} \right]^2, \tag{4.3}$$

where $U(z_P)$ is the velocity at the first cell centre, z_0 is the local surface roughness length, $\kappa = 0.4$ is the von Kármán constant, and Δz is the vertical distance to the wall. A Neumann condition is applied for turbulent kinetic energy k, and the production term in the wall cell is expressed as:

$$P_k = \tau_w \cdot \left[\frac{\ln\left(1 + \frac{\Delta z}{z_0}\right)}{\Delta z} \right]^2. \tag{4.4}$$

The dissipation rate ε is derived from equilibrium similarity theory:

$$\varepsilon = \frac{C_\mu^{3/4} k^{3/2}}{\kappa\,(z_0 + \Delta z)}. \tag{4.5}$$

The lateral boundaries are configured based on the incoming wind direction. The domain is aligned such that the side facing the wind is treated as an inflow, while the opposite side is treated as an outflow. The exact position of the inlet and outlet planes rotates with wind direction and is automatically determined based on sector definitions. For instance, as shown in Figure 4.5, a wind direction of 270° results in an outlet at 90°, with a range spanning ±22.5°.

The upper boundary is treated as a lid-driven inlet, where Dirichlet conditions are imposed for velocity and turbulence quantities. The prescribed profiles match those used at the lateral inflow, ensuring consistency in the representation of the incoming boundary layer. No condition is set for pressure at the top, allowing it to adjust freely to satisfy the momentum equations. This setup reflects the physical assumption that large-scale upper-layer flow drives the system, with momentum transferred downward through shear and turbulence rather than through vertical pressure gradients.

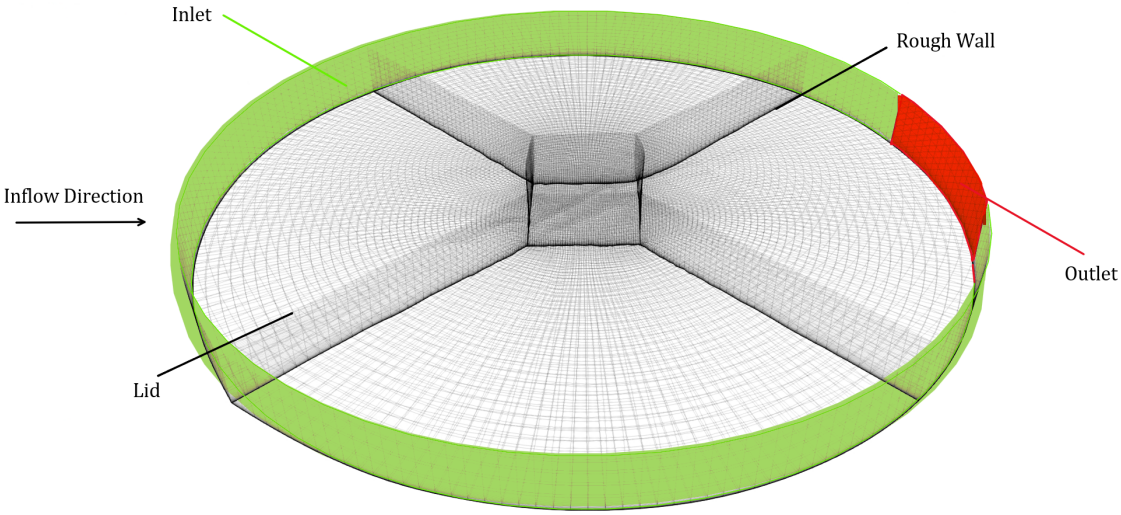

Figure 4.5: PyWakeEllipSys Boundary Conditions

4.2.2 *Initial Conditions*

In case of stable and unstable atmospheric conditions, the inflow profiles are generated using a 1D flat terrain precursor simulation, implemented via the `EllipSys1D` model in `PyWakeEllipSys`, introduced by van der Laan et al. (2017) [41]. This precursor solves a vertically resolved, horizontally homogeneous RANS formulation, yielding equilibrium profiles of wind speed $U(z)$, turbulent kinetic energy $k(z)$, and dissipation rate $\varepsilon(z)$. These are used to initialise the inflow velocity profile, improving the stability of the 3D RANS simulations by providing physically consistent inflow conditions.

The precursor uses the same rough wall boundary condition at the ground as previously presented and is run as a steady-state model [35], and is run using the `keMOB` turbulence model as introduced in Section 2.2. Precursor profiles are computed for both stable and unstable regimes based on the mean stability parameters derived in Section 3.5. One exception is the stable simulations due to solver stability reasons. This will be discussed in the next subsection.

The inflow velocity is normalised to $U_{ref} = 1$ m/s at $z_{ref} = 100$ m. As discussed in Section 2.1, this choice does not affect the resulting speed-up factors, which are computed relative to a reference wind speed and thus remain dimensionless.

Furthermore, since the roughness length at the inflow is a property of the terrain itself, the inflow TI_{ref} is set such that the roughness length remains constant using Equation 2.20. This is further explained in Section 2.2. An overview of the initial conditions of the simulation configurations is provided in Table 4.2.

Table 4.2: Summary of simulation run cases per stability regime.

Stability Class	**Turbulence Models**	TI_{ref}	ζ	$U(z_{ref})$	**Precursor**
Neutral	`ke`, `kefp`	0.16	0.00	1 m/s	No
Stable	`keMOB`, `keMOBfp`	0.13	0.25	1 m/s	Yes
Unstable	`keMOB`, `keMOBfp`	0.24	−0.42	1 m/s	Yes

4.2.3 *Simulation Execution*

RANS simulations are executed using `PyWakeEllipSys`, running EllipSys3D on DTU's GBar high-performance computing cluster. Each run is assigned a walltime of 9 hours and parallelised across 16 cores (two nodes). The solver advances in steady-state mode, using a convergence tolerance of 10^{-5} on the residual norm. Momentum and turbulence relaxation is set to the standard, except for the Obukhov models, where `relaxu` $= 0.7$ to improve convergence stability.

The grid configuration, described in Section 4.1, is kept fixed across all wind directions. Simulations are run for five directions from 230° to 250° in 5° increments, centred around 240°. This direction aligns with the primary valley axis and the orientation of mast booms, as described in Section 3.4, and represents the most frequent synoptic wind direction during the IOP.

For each inflow direction, the terrain simulations are conducted for all relevant combinations of turbulence model and atmospheric stability class. The standard k–ε model (`ke`), (`kefp`), and the Monin–Obukhov based models (`keMOB` and `keMOBfp`) are tested.

4.3 POST-PROCESSING

All simulation output is written in `netCDFmb` format and post-processed using custom scripts interfacing with the `xarray` and `numpy` libraries. Flow variables are interpolated at discrete mast locations (tse01, tse04, tse09, tse13) and along a horizontal transect connecting these masts. Interpolation is carried out on vertical profiles up to 100 m at 1 m resolution, for where the total wind speed and TI are determined as follows:

$$U = \sqrt{u^2 + v^2 + w^2} \tag{4.6}$$

$$TI = \frac{\sqrt{\frac{2}{3}k}}{U} \tag{4.7}$$

The reference wind speed U_{ref} at 30 m on the tse01 mast is used to normalise the profiles at each location, allowing for the computation of speed-up values as introduced in Section 2.1.

In order to handle the multiple wind directions that are simulated, the resulting profiles are combined into a single ensemble using weights representing the frequency of occurrence.

These weights are computed from the observed wind direction frequency distribution during the IOP (see Section 3.4).

Table 4.3: Wind direction weights applied during post-processing, based on frequency distribution at tse04 at 100 m.

Wind Direction (°)	**Respective Weight**
230.0 - 235.0	0.3079
235.0 - 240.0	0.2095
240.0 - 245.0	0.2381
245.0 - 250.0	0.2444

The post-processed datasets include the mean vertical profiles of wind speed, wind direction, and turbulence intensity. Results are saved to disk in plain-text tables for each mast and transect, and used directly in the validation procedure presented in Chapter 5. Figures illustrating the final modelled profiles are introduced in the next section.

5 RESULTS

This chapter presents the simulation results of RANS models over the Perdigão site. The evaluation covers speed-up factors, wind direction, and turbulence intensity, each compared against filtered measurement data as introduced in Chapter 3.

The results are first presented in Sections 5.1 and 5.2, where speed-up, wind direction, and TI are validated over a horizontal transect and by their vertical profiles at each mast. Streamline plots are then included in Section 5.3 to examine the flow behaviour in more detail.

Section 5.4 synthesises the findings across the different variables to assess model performance under varying atmospheric conditions. The effects of terrain, stability-dependent mixing, and turbulence modelling are discussed to provide a coherent interpretation of the simulation accuracy and its limitations.

5.1 HORIZONTAL TRANSECT

Figures 5.1, 5.2, and 5.3 show speed-up, wind direction, and turbulence intensity along the valley transect at $z = 100$ m a.g.l. for all different inflow models introduced in Section 4.2.

5.1.1 *Normalised Wind Speed Transect*

Under neutral conditions, flow accelerates moderately up the slope. The `ke` and `kefP` models appear to underpredict speed-up across the entire transect, aligning closely with the unstable simulation throughout.

Under stable stratification, speed-up starts above zero for $z = 100$ m a.g.l due to the normalisation based on the reference mast, which is measured at 30 m high. Upstream acceleration is more pronounced, slightly under-predicting the validation data on the first hilltop. Downstream from the first ridge, simulated speed-up remains consistently lower than the validation data.

For the unstable results, speed-up follows a similar trend up the first ridge. Past tse04, the flow decelerates in the valley but recovers rapidly, closely matching measurements at tse09 and tse13.

The `fP` variants consistently lower speed-up across the valley and downwind ridge. The reduction is strongest at tse09 and tse13 where the local turbulence length-scale limiter has the most significant impact.

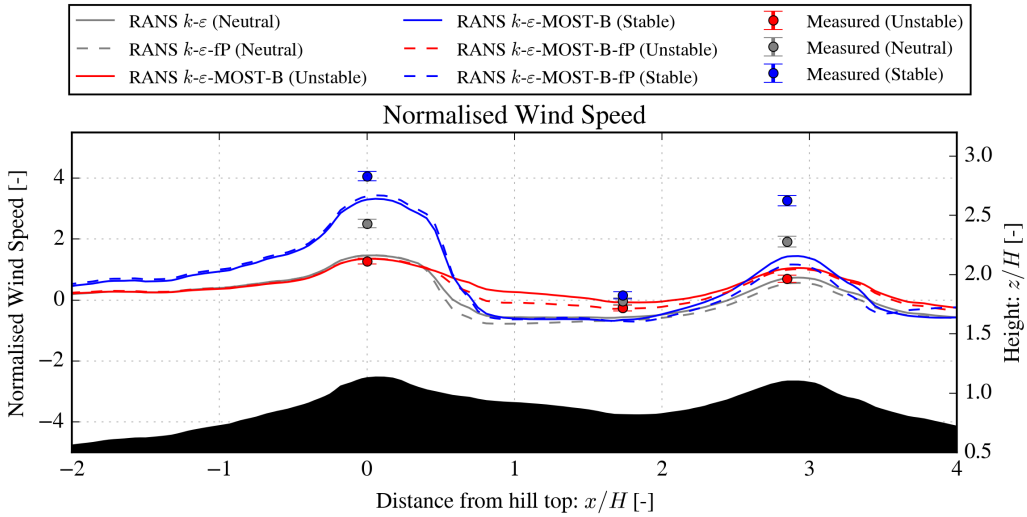

Figure 5.1: Normalised wind speed (w.r.t. $z = 30$ m a.g.l. at tse01) along the transect at $z = 100$ m a.g.l.

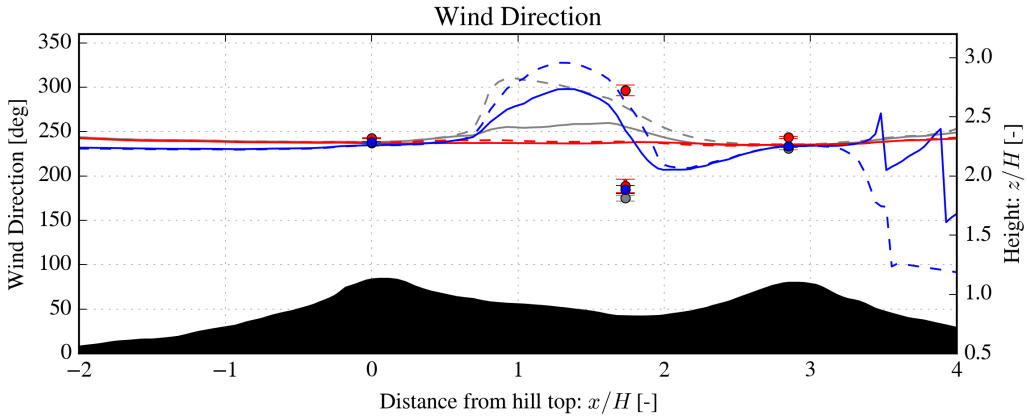

Figure 5.2: Wind direction along the transect at $z = 100$ m a.g.l.

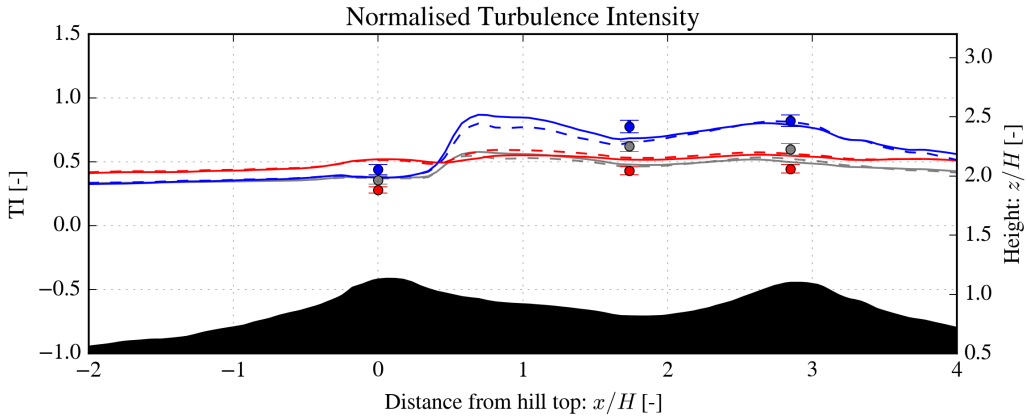

Figure 5.3: Normalised turbulence intensity (w.r.t. $z = 30$ m a.g.l. at tse01) along the transect at $z = 100$ m a.g.l.

5.1.2 *Wind Direction Transect*

In the neutral simulation, the wind direction varies substantially across the valley. Flow is deflected after the first ridge and does not stabilise before tse13.

Under stable conditions, the wind shows a similar pattern, though directional shifts appear more coherent. Flow remains misaligned inside the valley and is likely channelled or deflected by persistent near-surface recirculation. The recovery is partial by tse13, where the flow remains slightly offset from the inflow direction. After the second hilltop, the wind direction again changes rapidly.

In contrast, the unstable simulation shows little directional variation along the transect. Flow remains aligned with the inflow throughout, and no indication of either direction of the bimodal channelling found in the validation data appears at this height.

The `fP` variants broadly reproduce the same trends as their corresponding base models. However, directional shifts near suspected wake zones are more pronounced, particularly in the neutral and stable cases, which could reflect their increased wake persistence and slightly enhanced recirculation strength.

5.1.3 *Turbulence Intensity Transect*

In the neutral case, the model matches the measured turbulence intensity well at tse04. A notable increase appears just past the first hilltop, but TI is underpredicted at tse09 and tse13.

Under stable conditions, TI increases sharply after the first hilltop, forming the largest gradient across all cases. The values fit the measurements relatively well, with only slight underprediction at tse04 and good agreement at tse09 and tse13. The model captures both the trend and magnitude of the observed TI profile.

For the unstable case, TI is overpredicted at tse04 and remains consistently high across the transect. No clear increase occurs after the hilltop, and the simulation shows slight overprediction at tse09 and tse13.

The `fP` variants follow the same trends as their base models. The only noticeable difference is a less sharp TI increase under stable conditions, slightly smoothing the profile after the first hilltop without affecting the overall match with observations.

5.2 VERTICAL PROFILES AT MAST LOCATIONS

Figure 5.4 presents the vertical profiles of speed-up factor, TI and wind direction for each measurement height summarised in Table 3.2. The reference tower only measures at 10 m and 30 m, which provides extra information to interpret the results at the downstream masts.

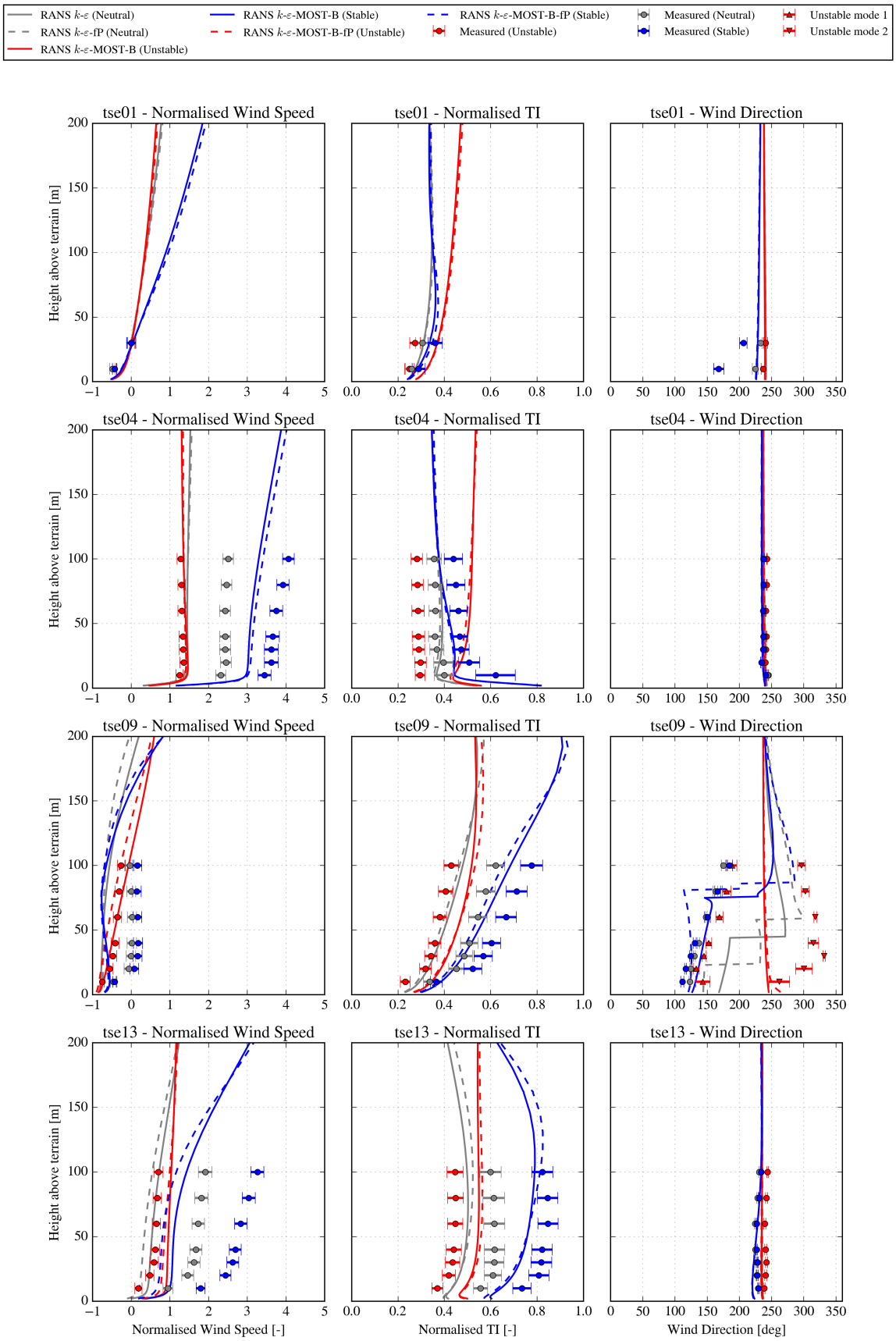

Figure 5.4: Vertical profiles of speed-up, turbulence intensity, and wind direction at each mast location. Left: speed-up factor, middle: Turbulence Intensity, right: Wind Direction.

5.2.1 *Normalised Wind Speed Profiles*

The left column presents the vertical normalised speed-up profiles at the four validation masts, relative to the reference velocity at tse01 at 30 m, consistent with the transect results.

At tse01, all models approach the defined inflow profile reasonably well, although the neutral simulation closely resembles the unstable case compared to the inflow profiles. The vertical shape of the profiles reflects the stability-dependent shear imposed by the inflow profiles, with stable conditions showing the strongest gradient.

At tse04, the speed-up is primarily governed by terrain effects and vertical shear. All simulations show similar profile shapes, with the unstable model matching measurements closely. The neutral simulation underpredicts across all heights, while the stable case slightly underpredicts above 60 m a.g.l. The difference between `fP` and base models remains small.

Further downstream, at tse09, all simulations predict reduced speed-up values near the surface, consistent with observed flow deceleration. The unstable model performs best, following the measured profile throughout the vertical. Both neutral and stable simulations underestimate speed-up, particularly below 80 m. The `fP` variants show a slightly stronger deceleration near the surface, suggesting enhanced wake persistence.

Finally, at tse13, located on the downwind ridge, the unstable simulation shows the best agreement with measured terrain-induced acceleration. The neutral and stable models underpredict speed-up throughout the profile, particularly below 100 m a.g.l., where terrain-driven acceleration is strongest. The differences between `fP` and non-`fP` models remain minor but show slightly reduced speed-up near the ridge crest.

5.2.2 *Turbulence Intensity Profiles*

The middle column presents the simulation results of intensity profiles at the validation masts. To enable meaningful comparisons between measurements and models, all TI values are normalised by the mean wind speed at tse01, consistent with the transect analysis. This avoids uncertainty from modelled local wind speeds and isolates the turbulence structure as a function of height.

First, at tse01, all models align reasonably well with measurements, although some deviations appear near the surface. The largest mismatch occurs under stable conditions, where modelled TI drops more rapidly with height compared to observations. Among the `fP` variants, the stable `keM0BfP` variant predicts a more pronounced increase in TI compared to the other `fP` variants.

At tse04, the neutral model underpredicts near the surface but converges to the measured profile above 60 m a.g.l. The stable simulation follows the vertical trend well up to around 80 m a.g.l, above which it begins to underpredict. The unstable model consistently overpredicts TI across the profile. The differences between the `fP` and non-`fP` variants are relatively

small at this point.

Furthermore, at tse09, measured TI increases with height and reaches its maximum at the upper levels. All simulations predict a much stronger vertical gradient. The neutral model strongly underpredicts TI at all heights. In contrast, both stable and unstable simulations follow the observed trend relatively well, capturing the increase in TI with height. The impact of the `fP` variant is small.

Finally, at tse13, the neutral model again underpredicts TI throughout the vertical, particularly between 40–100 m a.g.l. Both stable and unstable simulations capture the overall structure of the measured profile more accurately. The relative agreement with measurements is similar to tse09, suggesting that ridge-top wake recovery may be better captured in the stratified cases.

5.2.3 *Wind Direction Profiles*

In the left column, the vertical wind direction profiles at the four validation masts are presented. The results indicate how well the simulations reproduce terrain-induced flow curvature and directional shear under different stability conditions.

At tse01, a slight directional offset is observed near the surface across all measured conditions, which diminishes with height. All models show little to no variation in wind direction over height. This is especially the case for the stable validation data. Due to a lack of sensors above 30 m a.g.l. It is not possible to say how the wind behaves at higher altitudes.

Following for tse04, the measured wind direction remains nearly constant with height. The simulations capture this well across all stability regimes. The uniformity of the profile reflects the location's exposure to the faster incoming flow, which is not significantly altered by local terrain effects and small perturbations won't affect the flow much.

Next, at tse09, wind direction changes markedly with height under stable conditions. The stable simulation follows this trend relatively well, capturing the gradual turning. The neutral simulations follow a trend completely in the opposite direction, and unstable simulations fail to replicate much curvature, remaining closer to a uniform profile.

Finally, at tse13, wind direction is again nearly uniform across height in both measurements and simulations. Minor deviations are observed under stable conditions. This is present but much less pronounced in the observations.

5.3 DETAILED FLOW PATTERNS

This section examines the underlying flow structures that drive the observed speed-up and wind direction patterns. Vertical and horizontal streamline plots are used to visualise terrain-induced recirculation, flow separation, and wake recovery behaviour across stability regimes. Results for the `fP` model variants are provided in Appendix A.2.

5.3.1 *Vertical Streamline Patterns*

Vertical streamline and speed-up patterns across different stability conditions are illustrated in Figure 5.5. Streamline lifting over the ridge clearly shows terrain-induced vertical flow displacement with noticeable flow separation and a recirculation zone behind the first ridge. Stable conditions show an elongated downstream recirculation zone, reaching the second ridge. Unstable conditions tend to enhance wake recovery through intensified vertical mixing, reducing recirculation size and strength, consistent with faster wake dissipation observed in literature [19].

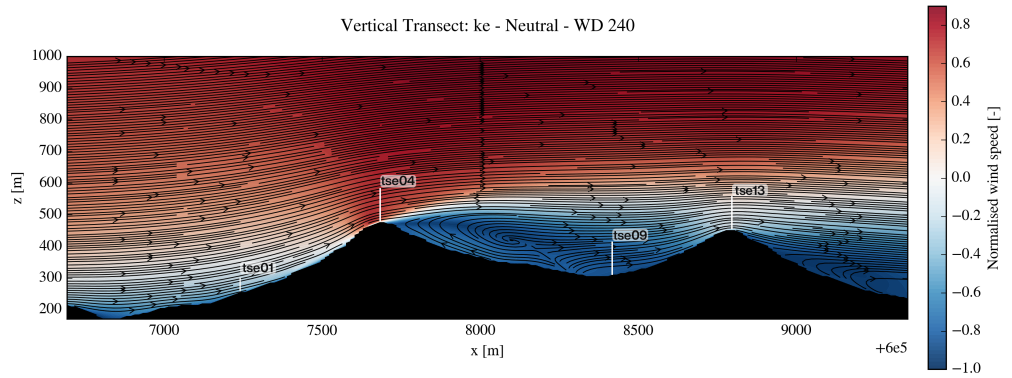

(a) Neutral stability, ke

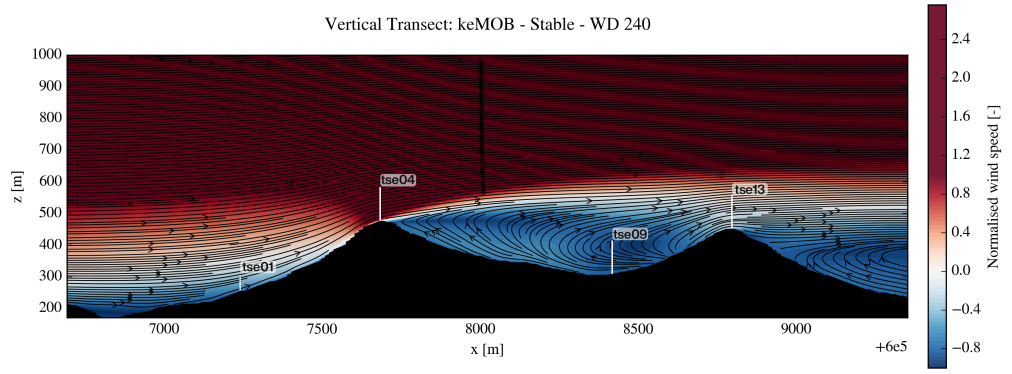

(b) Stable stability, keMOB

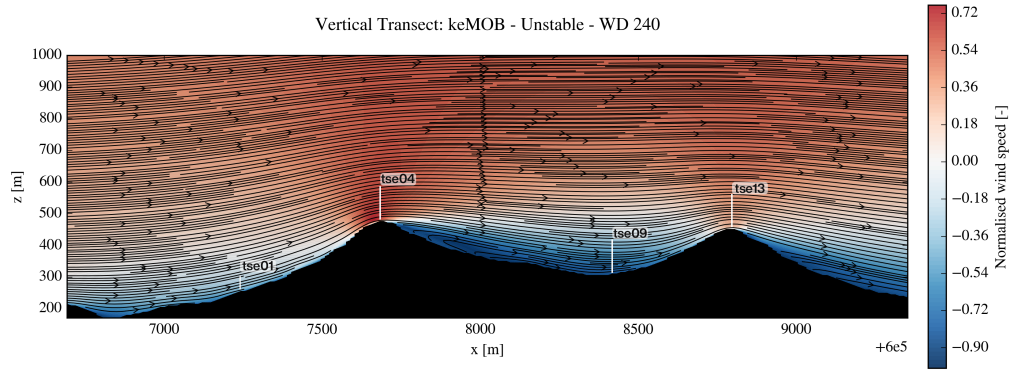

(c) Unstable stability, keMOB

Figure 5.5: Vertical streamline and speed-up patterns for different stability conditions.

5.3.2 *Horizontal Streamline Patterns*

Horizontal flow patterns at 100 m a.g.l. of mast tse09 are shown in Figure 5.6. Persistent recirculation across all regimes can be observed. Under stable conditions, the recirculation zone is developed and extends further downstream. In the neutral case, the recirculation footprint is shorter and more confined, while under unstable conditions, the flow reattaches rapidly after the first ridge. This suggests that although recirculation is a consistent feature in the valley, the 100 m level intersects its upper boundary under unstable and, to some extent, neutral conditions. In contrast, for stable flow, the recirculation remains well developed at this height.

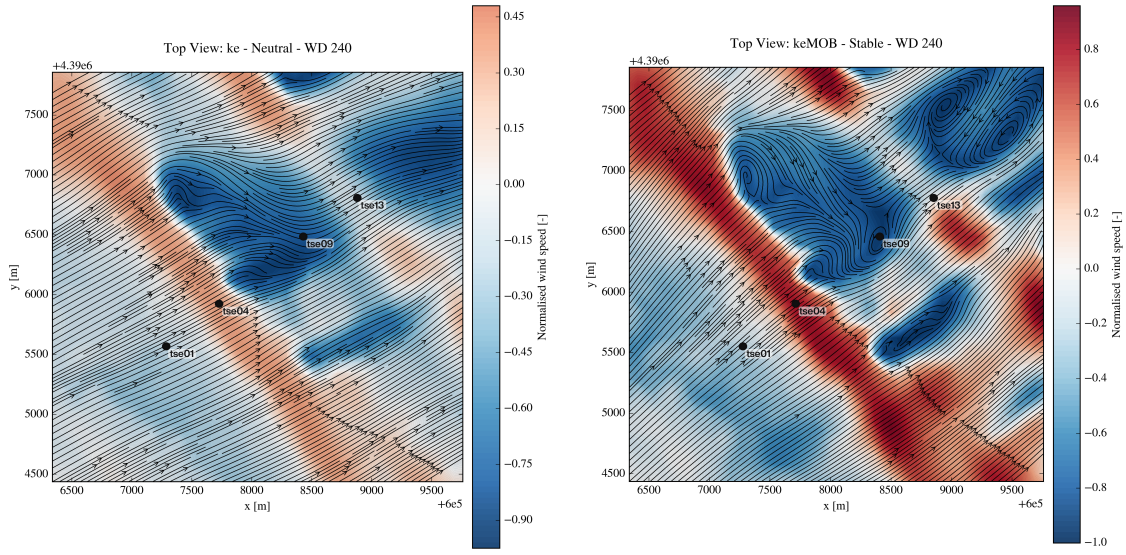

(a) Neutral stability, ke

(b) Stable stability, keMOB

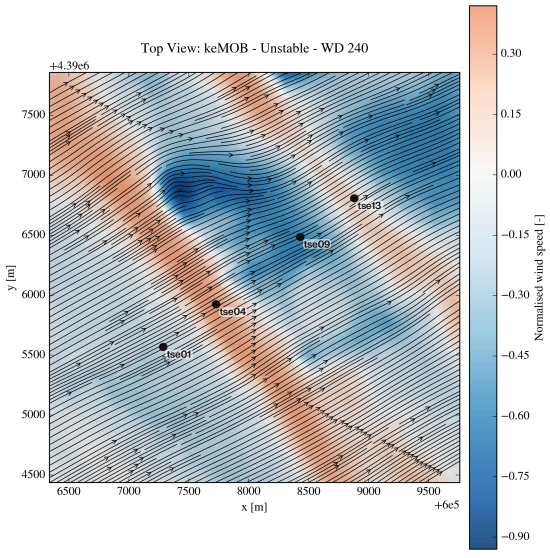

(c) Unstable stability, keMOB

Figure 5.6: Horizontal streamline and speed-up patterns at 100 m a.g.l. near mast tse09.

5.4 INTERPRETATION OF RESULTS

5.4.1 *Speed-up and Wake Recovery*

On the upwind ridge, the simulated speed-up is primarily governed by terrain-induced acceleration and vertical shear, rather than wake effects. This is consistent with Figure 5.1, where flow separation is not yet present, and the flow remains attached to the slope. Surprisingly, the neutral simulation behaves similarly to the unstable simulations, both in speed-up magnitude and vertical profile shape, without an obvious physical explanation. This resemblance is most likely due to similar vertical shear structures up to 100 m a.g.l., as confirmed by the reference mast speed-up profiles.

The underprediction of speed-up at the valley mast tse09 for neutral and stable conditions arises mainly from persistent simulated wake structures. These extended recirculation zones, evident from Figures 5.5 and 5.6, hinder wake recovery at 100 m a.g.l., contrasting with observational data that suggest the flow at this height is already recovering. In the unstable simulations, enhanced turbulent mixing results in higher dissipation rates, aligning with documented findings that instability promotes shorter wake lengths and improved recovery in complex terrain [19]. This interpretation is further supported by turbulence intensity profiles (Figure 5.4), where both unstable and stable simulations closely replicate measured turbulence profiles.

Notably, the stable case captures the observed TI well despite underpredicting speed-up. This decoupling aligns with the findings of van der Laan et al. (2023), who showed that velocity recovery in wakes is governed by the divergence of Reynolds shear stresses, specifically $\partial u'v'/\partial y$ and $\partial u'w'/\partial z$, rather than by the turbulence intensity or mean shear alone [39]. Accurate modelling of these stress divergence terms is sufficient to reproduce mean velocity profiles, even when turbulence levels are misrepresented. Conversely, matching TI profiles does not guarantee correct mean flow recovery, especially in regions dominated by pressure gradients or adverse terrain effects, where velocity recovery depends more sensitively on how momentum is transported across the wake or terrain-induced shear layers.

On the downwind ridge, underpredictions persist in the stable and neutral cases. While wind direction profiles are reasonably captured, the speed-up values remain too low compared to measurements. Figure 5.5 reveals that in these cases, the wake originating from the upstream ridge remains present as the flow approaches the second ridge top, limiting the speed-up that can develop over the second ridge. However, in the unstable simulation, the flow arrives relatively undisturbed, which is consistent with the better match to the observed acceleration at this site. This again suggests that the differences in mixing strength and recovery length inherent to each stability regime play an important role in shaping the accuracy of the RANS model predictions at this site.

5.4.2 *Wind Direction Structure*

At tse01, a near-surface directional shift is present in all measurement data, which rapidly recovers with height. At the ridge-top masts tse04 and tse13, wind direction remains relatively constant with height, and model predictions closely follow observations.

Inside the valley, only the stable case captures the observed directional trend with height. The other models deviate substantially, suggesting a challenge of resolving valley recirculation zones and wake-induced deflections. Despite the strong overall performance of the unstable `keMOB` turbulence model in speed-up and turbulence intensity, the unstable wind direction results differ significantly from measured directional modes, particularly within the valley. The measured bimodal structure observed at tse09 under unstable conditions (Figure 3.11), or for that matter, the consistent ridge-parallel south-east directions in other stability regimes, seems not to be captured by the simulations. Knowing the absence of significant circulation evident at this height under unstable conditions, these directional discrepancies should theoretically arise from forced channelled flows within the valley: an effect documented in theoretical studies of ridge-valley systems, but inherently challenging for steady-state RANS models to capture accurately [19].

5.4.3 *Turbulence Intensity and Mixing Representation*

Turbulence intensity profiles provide further insight into modelled mixing strength. The unstable simulations closely replicate measured turbulence profiles at the stations after the first hill top, indicating accurate representation of wake dissipation and turbulence redistribution under convective conditions. At the upwind ridge, the unstable case consistently overpredicts turbulence, while the stable and neutral simulations match the measured profile more closely.

At tse09 and tse13, the neutral simulation significantly underpredicts TI throughout the profile, suggesting insufficient turbulence production in zones of high shear and recirculation. In contrast, both stable and unstable simulations capture the vertical structure of TI relatively well. Taken together with the speed-up results, this implies that accurate turbulence reproduction does not seem to guarantee accurate wind speed predictions. Indicating that in this case, speed-up is more sensitive to wake advection and pressure gradients, whereas TI primarily reflects local mixing and shear generation.

5.4.4 *Cross-Variable Interpretation and Model Implications*

Combining the findings across speed-up, wind direction, and turbulence intensity allows for a detailed analysis of the capabilities and limitations of the simulations. The unstable Monin–Obukhov turbulence model (`keMOB`) consistently produces realistic speed-up and turbulence distributions, confirming accurate simulation of wake dimensions and intensities. However, it fails to capture observed directional modes in the valley, suggesting missing mechanisms such as forced channelled flow.

For stable conditions, while wind direction is generally well-predicted, the consistent underestimation of speed-up highlights a weakness in modelling the intensity and spatial extent of terrain-induced wakes under suppressed turbulent mixing. Neutral simulations perform inconsistently across all measured parameters, possibly due to their sensitivity to small variations in local mixing and the relatively variable nature of neutral stratification during the IOP.

5.5 DISCUSSION

5.5.1 *Interpretation with Theory and Literature*

The observed and simulated flow behaviour at the Perdigão site can be further interpreted in light of known theoretical concepts describing valley flows. Figure 3.7 illustrates several possible microscale processes in an idealised 2D valley. This conceptual framework helps to distinguish which physical processes are expected to occur and which of them are resolved, or fundamentally unresolved by steady-state RANS modelling.

A number of key features in the figure correspond well with the flow phenomena observed in the simulations. Flow separation on the upwind slope and the formation of recirculation zones are visible in both vertical and horizontal streamline plots (Figure 5.5, Figure 5.6). These are features that RANS models can generally capture. The size and strength of the simulated recirculation zones vary across stability regimes, consistent with known theoretical expectations: stable conditions suppress vertical mixing and increase recirculation length, while unstable conditions enhance turbulent exchange and accelerate (shorten) wake recovery [19].

Coherent structures and shear layers, such as those shown developing along valley sidewalls also seem to be approximated in RANS in a time-averaged sense. These are resolved as velocity gradients and turbulence intensity peaks, but their fluctuating nature and time-dependent variability are inherently smoothed out. Similarly, terrain-induced speed-up and subsidence over ridge crests are features that are well captured in the simulation data, especially with limited wake effects under unstable stratification, where the Monin–Obukhov-enhanced model provides the most accurate reproduction of measured flow acceleration.

However, several processes that may be occurring in real life are outside the capability of steady-state RANS. Most notably, unsteady thermally-driven flows such as katabatic and anabatic winds are not resolved. These are time-evolving phenomena governed by surface heat fluxes and buoyancy effects, which require transient or coupled radiation–surface–atmosphere models to simulate accurately. The influence of thermally forced valley flows, often responsible for directional variability, is therefore largely absent in the current simulations, which could partly explain the inability to capture bimodal forcing winds inside the valley.

Additionally, dynamic features cannot be resolved in steady-state simulations. These are inherently transient and often sensitive to small-scale surface heterogeneities, stratification

gradients, and time-varying boundary conditions. Their absence limits the model's ability to predict localised turbulence spikes, pressure-driven flow reversals, and directional instabilities in double ridge environments like Perdigão.

Finally, the results show that terrain-induced complexity arises not only from the geometry but also from the interaction between synoptic forcing and mesoscale atmospheric stability. Since the RANS setup used here employs fixed inflow profiles and assumes steady atmospheric conditions, the simulation represents an equilibrium state rather than a dynamic evolution.

5.5.2 *Implications for Wind Energy Applications*

The results of this study present insights relevant to wind energy planning and turbine siting in complex terrain. Firstly, the inclusion of multiple atmospheric stability regimes offers a more complete picture of wind speed and turbulence variability, especially in terrain-induced flow systems. Since long-term wind energy yield and turbine loading are strongly influenced by variations in TI, evaluating flow behaviour under stable, neutral, and unstable stratifications allows for a more realistic classification of operational conditions than a purely neutral model.

Although valley flows, such as those observed at tse09, are unlikely to host wind turbines directly due to low wind speeds, directional instability, and high turbulence, accurately resolving their behaviour can remain useful. Recirculation zones can have significant downstream impacts, particularly on turbines placed on downstream areas. As shown in this study, unresolved wakes and insufficiently dissipated turbulence can propagate downstream, reducing the effectiveness of terrain acceleration and increasing turbulence levels at locations that might otherwise seem promising. Understanding whether such flow structures exist, and whether they are likely to persist under specific stability conditions, is therefore helpful in evaluating the long-term viability of a site.

Furthermore, the underprediction of speed-up and overprediction of TI by some turbulence models shows the importance of model selection and validation in wind resource assessment. If not properly validated, models such as $k-\varepsilon$ may underestimate annual energy production or overestimate fatigue loading, leading to conservative or suboptimal siting decisions.

Finally, modelling results like those presented here can inform the layout and orientation of wind farms in complex regions. For example, recognising which stability regimes dominate during energy-producing hours can influence not only siting decisions, but also expectations of wake recovery and turbine interactions. Sites with dominant unstable conditions may support placing wind turbines that would otherwise be affected by wakes in stable or neutral conditions, and vice versa. These results ultimately provide a more informed, physics-based approach to wind farm design in complex terrain.

6

GRID CONVERGENCE STUDY

This chapter employs a mixed-order extrapolation approach to quantify numerical discretisation errors arising from grid resolution. The method builds on the framework of Roy (2003) [51], which extends classical Richardson extrapolation by accounting for first- and second-order truncation errors. This is particularly relevant in terrain-resolved RANS simulations, where local flow complexity may not follow monotonic convergence behaviour.

6.1 NUMERICAL SETUP

Five structured grids were generated, each varying the number of cells per rotor diameter D in the inner domain: $\Delta = D/1, D/2, D/4, D/8$, and $D/16$. All simulations were performed using the k–ε turbulence model and fixed grid dimensions consistent with the setup described in Chapter 4. The simulation inflow direction was fixed at 240°, corresponding to the dominant valley-aligned wind direction during the IOP. For each resolution, speedup profiles were extracted at the mast locations tse04, tse09, and tse13, and interpolated to a common vertical grid based on the finest mesh ($\Delta = D/16$).

The mixed-order extrapolation follows the functional form:

$$f(h) = f_0 + g_1 h + g_2 h^2, \tag{6.1}$$

where $f(h)$ is the computed solution at grid spacing h, f_0 is the extrapolated solution at zero grid spacing, and g_1, g_2 denote the first- and second-order error coefficients, respectively. The fit is performed independently at each vertical level using a weighted least-squares regression. Discretisation error at each grid level is then defined as:

$$\epsilon(h) = f(h) - f_0, \tag{6.2}$$

allowing a direct quantification of the local resolution error relative to the extrapolated zero-grid limit. To complement the accuracy analysis, computational cost was also estimated for each grid resolution based on CPU time as described in Equation 6.3:

$$\text{CPU Time} = \text{Total Run Time} \times N_{CPU} \tag{6.3}$$

Table 6.1 summarises the total number of cells and the CPU Time for a single $k - \varepsilon$ simulation.

6.2 RESULTS AND ANALYSIS

Two sets of figures are used to evaluate convergence trends. Figure 6.1 shows a speedup profile extracted along a horizontal transect crossing the hilltop, with the associated discretisation errors shown below. Results indicate that coarse grids ($\Delta = D/1, D/2$) significantly under-resolve flow separation and recirculation features, whereas the finer grids ($\Delta = D/8$,

Table 6.1: CPU time per grid resolution.

Resolution	Number of Cells	CPU Time [s]
$\Delta = D/1$	1105920	1384
$\Delta = D/2$	2654208	3925
$\Delta = D/4$	7077888	33859
$\Delta = D/8$	17031168	241332
$\Delta = D/16$	55738368	1970022

D/16) closely approximate the mixed-order extrapolated profile. Discretisation error reduces substantially with increasing resolution, particularly in regions of steep terrain slopes and high shear gradients.

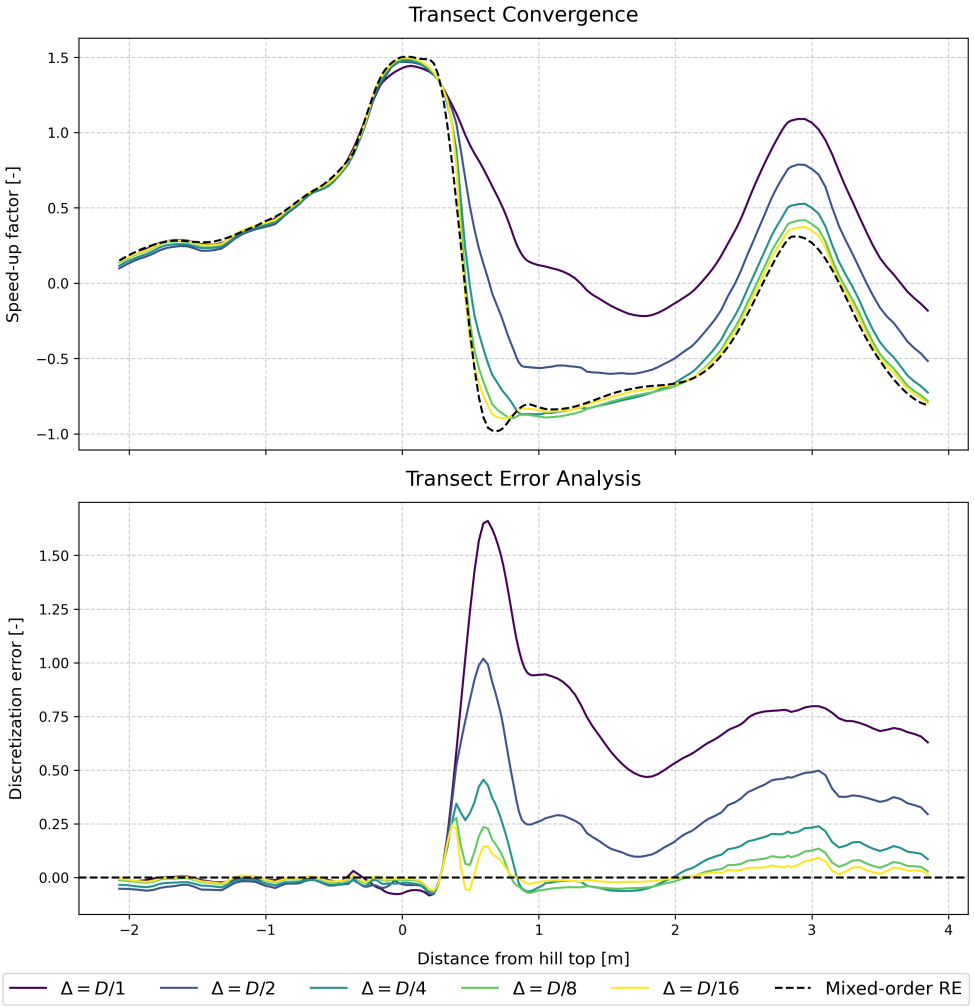

Figure 6.1: Top: speedup factor along transect line for each grid resolution. Bottom: local discretisation error with respect to extrapolated mixed-order solution.

Figure 6.2 presents vertical speedup profiles and error estimates at the three mast locations. At tse04, which lies on the upwind ridge, all resolutions converge smoothly with minor discrepancies, consistent with its relatively simple flow regime. At tse09, located in the valley, convergence is poor at low altitudes due to strong recirculation and terrain-induced turbulence. Above 100 m, however, the different profiles collapse, indicating acceptable resolution at rotor-relevant heights. At tse13, positioned on the downwind ridge, convergence is again slower, especially near the surface, reflecting the influence of terrain-induced acceleration and wake effects.

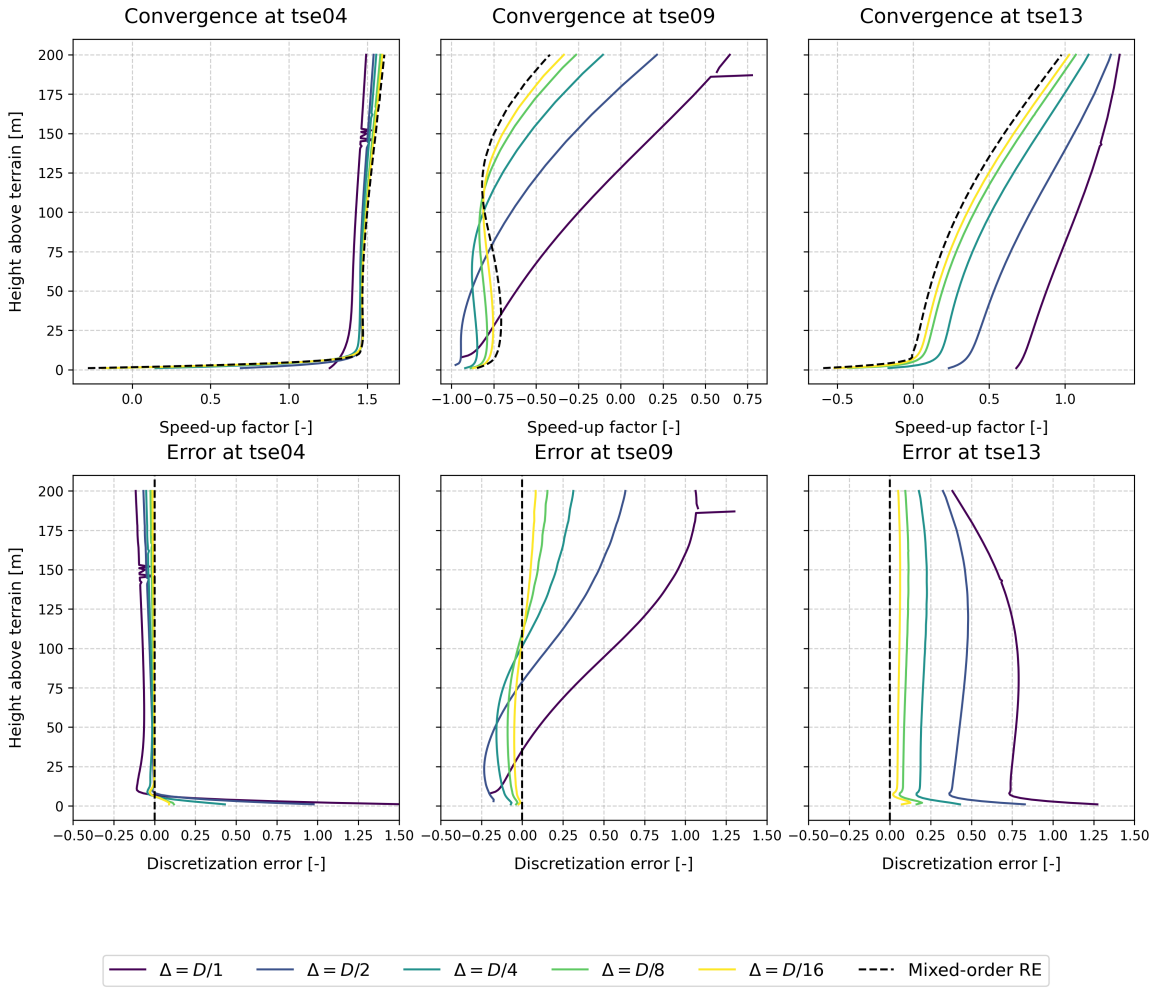

Figure 6.2: Top: vertical speedup profiles at each mast location for all grid resolutions. Bottom: corresponding discretisation errors with respect to extrapolated mixed-order solution.

The analysis confirms that grid resolution exerts a strong influence on predicted flow fields, particularly in terrain-induced recirculation zones and near-surface shear layers. While finer grids do provide better agreement with the extrapolated solution, gains beyond $\Delta = \mathrm{D}/8$ are marginal at turbine-relevant heights, suggesting a reasonable trade-off between accuracy and computational cost. Therefore, for this study a grid spacing of $\Delta = \mathrm{D}/8$ represents an effective balance between computational cost and predictive accuracy.

7

CONCLUSION

In this thesis, the predictive capabilities of RANS-based CFD simulations in PyWakeEllipSys over complex terrain, for the Perdigão field campaign, were evaluated. The core aim was to assess whether steady-state RANS models, under realistic meteorological and topographical conditions, can reproduce observed speed-up factors, turbulence intensity profiles, and wind direction patterns with sufficient accuracy for wind resource assessment. The results show that while the models capture several key flow phenomena, some limitations remain in their ability to resolve directional variability and flow structures within the valley.

The validation against vertical and horizontal measurements confirms that PyWakeEllipSys is capable of reproducing the magnitude and spatial distribution of speed-up over the ridge–valley system. The unstable `keMOB` turbulence model yielded the best agreement in terms of speed-up and turbulence profiles. At the same time, the stable model was shown to perform well in representing turbulence intensity at the valley mast, but consistently underpredicted speed-up across the transect, induced by heavy modelled flow circulation patterns. This divergence indicates that good TI representation does not necessarily imply correct velocity prediction, and vice versa. In neutral conditions, the model showed less accurate performance for all quantities.

The inclusion of Monin–Obukhov stability corrections (`MOB`) and the local turbulence length-scale limiter (`fP`) introduced relevant effects in regions of recirculation and strong shear, altering wake persistence and TI recovery. Originally developed for modelling wind turbine wakes, the `fP` variant consistently produced larger and more persistent recirculation zones in complex terrain. While this led to improved near-surface TI agreement in some cases, compared to the validation data, these models performed generally less accurately than their non-`fP` counterparts.

Validation of wind direction revealed that RANS models reproduce height-dependent trends on ridge tops and at the reference mast but fail to capture observed flow modes in the valley. In particular, the measured bimodal directional behaviour under unstable conditions could not be reproduced by any model variant. The steady-state framework does not support forced directional switching or dynamic channelled flow, which are time-dependent and potentially multi-modal in nature. These limitations are consistent with the expected capabilities of RANS models and point toward the need for transient modelling or alternative methods for capturing valley-scale directional variability.

The broader research question, whether PyWakeEllipSys can accurately reproduce observed flow over complex terrain, can be answered in parts. The simulations capture the spatial patterns of speed-up and turbulence reasonably well, particularly under unstable stratification. However, directional variability in the valley and interactions between terrain-induced

wakes and atmospheric stability remain challenging to model.

Several new questions have emerged from this work. The role of transient flow behaviour, such as directional switching or topographically induced lee waves, remains unexplored in this context. Similarly, the accuracy of precursor inflow profiles in reproducing vertical turbulence structures could be studied further, particularly under neutral conditions. Investigating the benefit of ensemble approaches or higher-order models such as LES, selectively applied to ridge–valley transects, may provide new insight into flow dynamics that remain out of reach for steady-state RANS.

In the context of the European TPWind "3% vision," the results presented here support the feasibility of using RANS-based CFD models to reduce uncertainty in wind resource assessment, provided their limitations are well understood and validation is performed under representative conditions. The modelling framework used in this thesis offers a strong basis for continued research and a practical tool for complex terrain wind modelling when combined with site-specific data and targeted validation.

7.1 FUTURE WORK AND RECOMMENDATIONS

This study has demonstrated that even well-established steady-state RANS models can struggle to reproduce wind field characteristics in terrain as complex as the Perdigão site, particularly under stable and neutral stratification. While the unstable case was generally reproduced well using the `keMOB` model, several important limitations were encountered, especially in resolving wake persistence, turbulence distribution, and directional variability in the valley. The following recommendations aim to guide further research that builds upon and critically addresses these shortcomings.

INTRODUCE TRANSIENT ABL MODELLING WITH DIURNAL FORCING. A natural next step in modelling is to incorporate time-dependent effects, particularly those governing the evolution of the atmospheric boundary layer over a day. The use of a transient RANS framework, such as the `keABLdc` model available in EllipSys [38], offers the capability to simulate the diurnal cycle via an idealised time-varying heat flux boundary condition. Such a setup would better reflect the transient character of the real atmosphere and may lead to more accurate predictions of directional variability and flow asymmetries in the valley, particularly at transitional times such as morning and evening (neutral). Although this introduces computational cost beyond steady-state RANS, it remains several orders of magnitude cheaper than LES and is an attractive intermediate solution [52].

USE LES SELECTIVELY AND CRITICALLY. While Large Eddy Simulation is often proposed as an alternative to RANS, such recommendations require context. For Perdigão, LES has shown promise in resolving terrain-induced flow variability, turbulence anisotropy, and directional shifts, particularly under varying stability regimes. Studies such as Berg et al. (2018) [7] applied WRF-LES to simulate realistic diurnal transitions and stratification effects. However, accurate LES of stability-driven flow requires fine vertical resolution, realistic surface forcing, and large domains, which limits its accessibility for full-site long-duration simulations. A selective LES approach could be interesting. Focused simulations of the

main valley transect under idealised stable and unstable conditions could resolve wake development, reattachment, and directionality shifts, while remaining computationally feasible. These configurations remain underexplored and offer a way to isolate key processes that steady-state RANS cannot capture. In this context, LES should complement rather than replace RANS. Motivating investigation of time-dependent stability effects and subgrid turbulence structures.

LEVERAGE LIDAR DATA FOR FUTURE VALIDATION. This study relied on met mast data, but the Perdigão site also features an extensive network of scanning and long-range lidars. Lidar transects capture flow curvature, wake deformation, and jet structures across ridges and valleys. Future work could incorporate lidar-based radial velocity or reconstructed wind fields into the validation workflow, enabling better constraints on modelled flow patterns, especially those outside of mast locations, such as in flow convergence regions or above ridge crests. In addition, lidar data could help identify diurnal flow patterns or low-level jets that are currently unrepresented in steady-state RANS simulations.

TEST MODEL PERFORMANCE AT OTHER COMPLEX SITES. Perdigão is a uniquely challenging case due to the enclosed double ridge and frequent directional variability, which may limit the generalisability of conclusions. To broaden the evaluation of RANS turbulence closures, future studies should consider additional sites with well-characterised measurement campaigns. One suitable candidate is the Alaiz site in Spain, which features rugged topography with open ridge configurations, fewer valley-induced directional shifts, and extensive met mast and remote sensing instrumentation as part of the NEWA measurement campaign [10].

DEVELOP PROBABILISTIC ASSESSMENT FRAMEWORKS. Finally, future research could move towards quantifying uncertainty in complex-terrain simulations. This includes both model-form uncertainty (turbulence model choice, parameter tuning) and input uncertainty (inflow profiles, surface roughness). Probabilistic frameworks, including ensemble-based RANS approaches or surrogate modelling with uncertainty quantification, would allow model results to be interpreted with confidence intervals to assess risk more systematically.

A

APPENDIX

A.1 LAND-COVER CLASSIFICATION AND SURFACE PARAMETERS

Table A.1: Land-cover type, roughness length z_0, displacement height d, and description [17].

id	z_0 (m)	d (m)	Description
0	0.0000	0.0	No data
10	0.1000	0.0	Cropland, rainfed
11	0.1000	0.0	Cropland rainfed, Herbaceous cover
12	0.2000	0.0	Cropland rainfed, Tree or shrub cover
20	0.0500	0.0	Cropland, irrigated or post-flooding
30	0.2000	0.0	Mosaic cropland (>50%) / natural vegetation (<50%)
40	0.3000	0.0	Mosaic natural vegetation (>50%) / cropland (<50%)
50	1.5000	0.0	Tree cover, broadleaved, evergreen
60	1.0000	0.0	Tree cover, broadleaved, deciduous
61	1.0000	0.0	Tree cover, broadleaved, deciduous, closed (>40%)
62	0.8000	0.0	Tree cover, broadleaved, deciduous, open (15–40%)
70	1.5000	0.0	Tree cover, needleleaved, evergreen
71	1.5000	0.0	Tree cover, needleleaved, evergreen, closed (>40%)
72	1.5000	0.0	Tree cover, needleleaved, evergreen, open (15–40%)
80	1.2000	0.0	Tree cover, needleleaved, deciduous
81	1.2000	0.0	Tree cover, needleleaved, deciduous, closed (>40%)
82	1.2000	0.0	Tree cover, needleleaved, deciduous, open (15–40%)
90	1.5000	0.0	Tree cover, mixed leaf type
100	0.2000	0.0	Mosaic tree and shrub (>50%) / herbaceous cover (<50%)
110	0.1000	0.0	Mosaic herbaceous cover (>50%) / tree and shrub (<50%)
120	0.1000	0.0	Shrubland
121	0.2000	0.0	Shrubland evergreen
122	0.2000	0.0	Shrubland deciduous
130	0.0300	0.0	Grassland
140	0.0100	0.0	Lichens and mosses
150	0.0500	0.0	Sparse vegetation (<15%)
151	0.0500	0.0	Sparse tree (<15%)
152	0.0500	0.0	Sparse shrub (<15%)
153	0.0500	0.0	Sparse herbaceous cover (<15%)
160	0.8000	0.0	Tree cover, flooded, fresh or brackish water
170	0.6000	0.0	Tree cover, flooded, saline water
180	0.1000	0.0	Shrub or herbaceous cover, flooded, fresh/saline/brackish water
190	1.0000	0.0	Urban areas
200	0.0050	0.0	Bare areas
201	0.0050	0.0	Consolidated bare areas
202	0.0050	0.0	Unconsolidated bare areas
210	0.0000	0.0	Water bodies
220	0.0030	0.0	Permanent snow and ice

A.2 FP VARIANTS OF STREAMLINE PLOTS

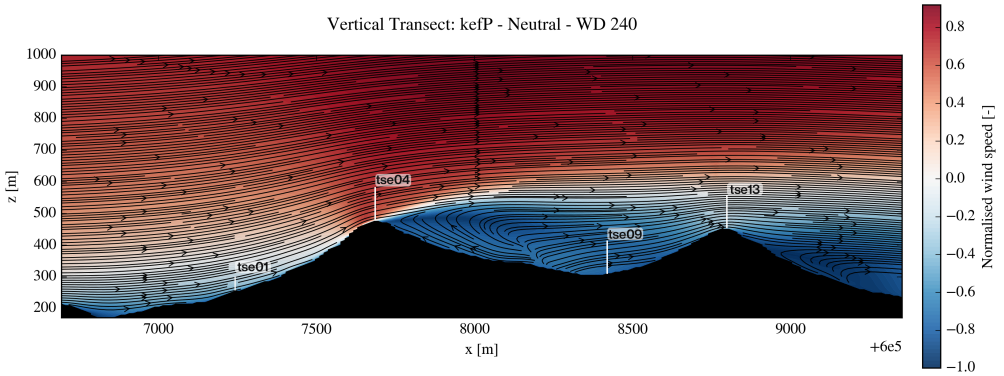

(a) Neutral stability, kefP

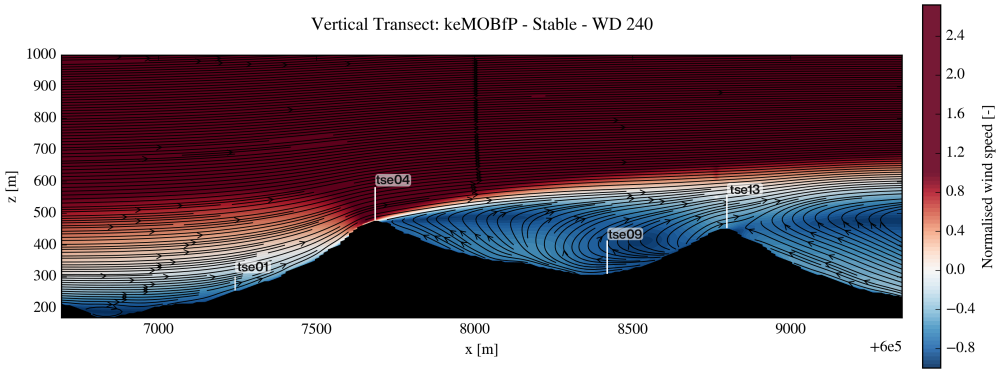

(b) Stable stability, keMOBfP

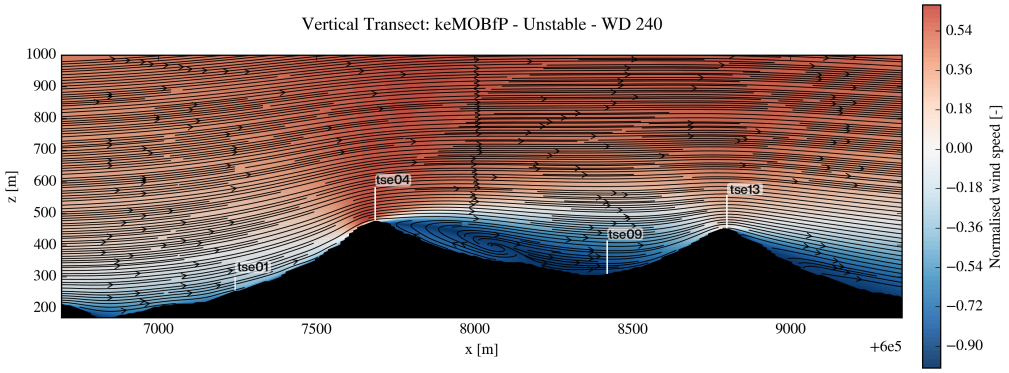

(c) Unstable stability, keMOBfP

Figure A.1: Vertical streamline and speed-up patterns for different stability conditions.

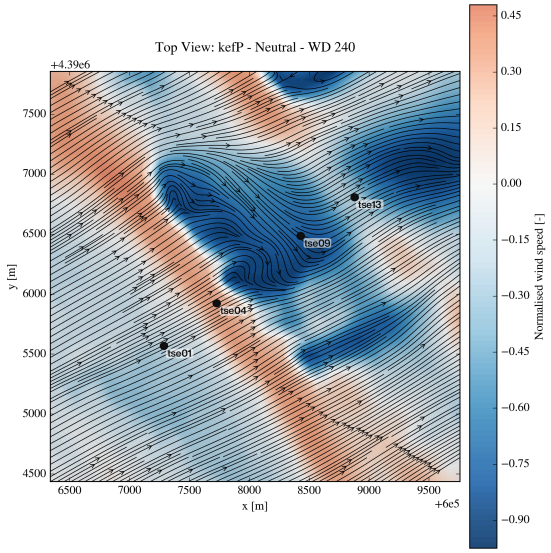

(a) Neutral stability, kefP

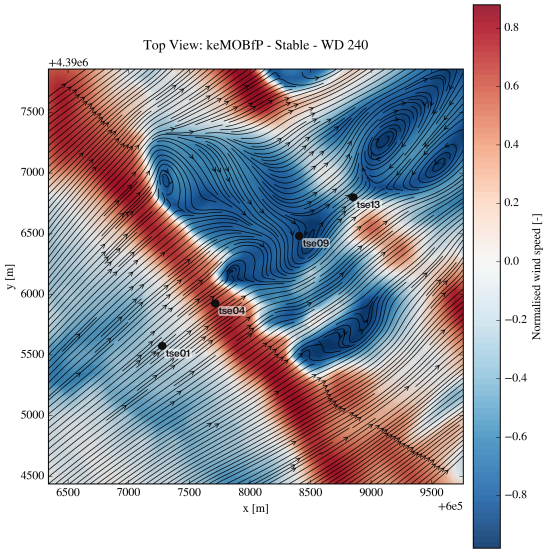

(b) Stable stability, keMOBfP

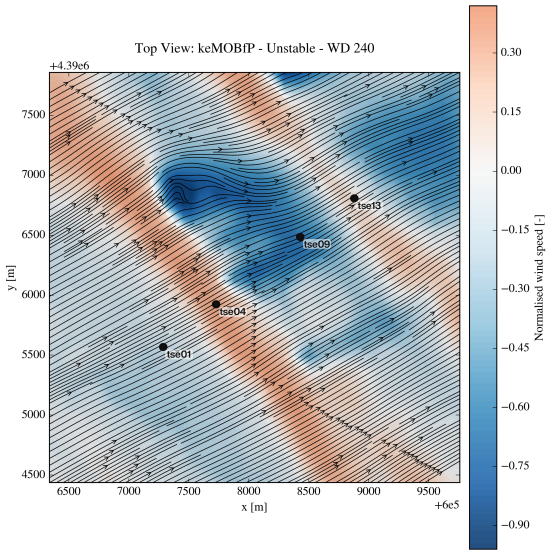

(c) Unstable stability, keMOBfP

Figure A.2: Horizontal streamline and speed-up patterns at 100 m a.g.l. near mast tse09.

B

PYTHON CODE FLOW CHARTS

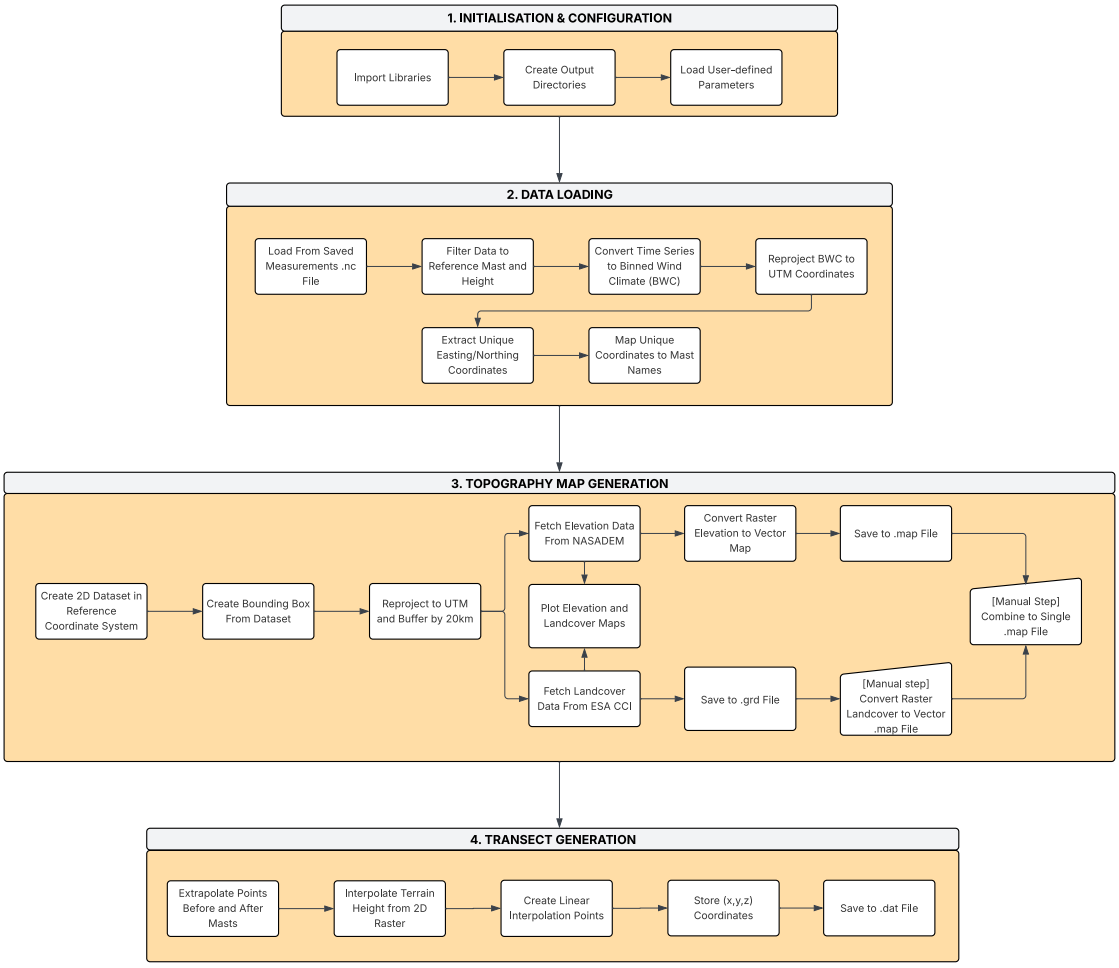

Figure B.1: Site_description.py flow chart

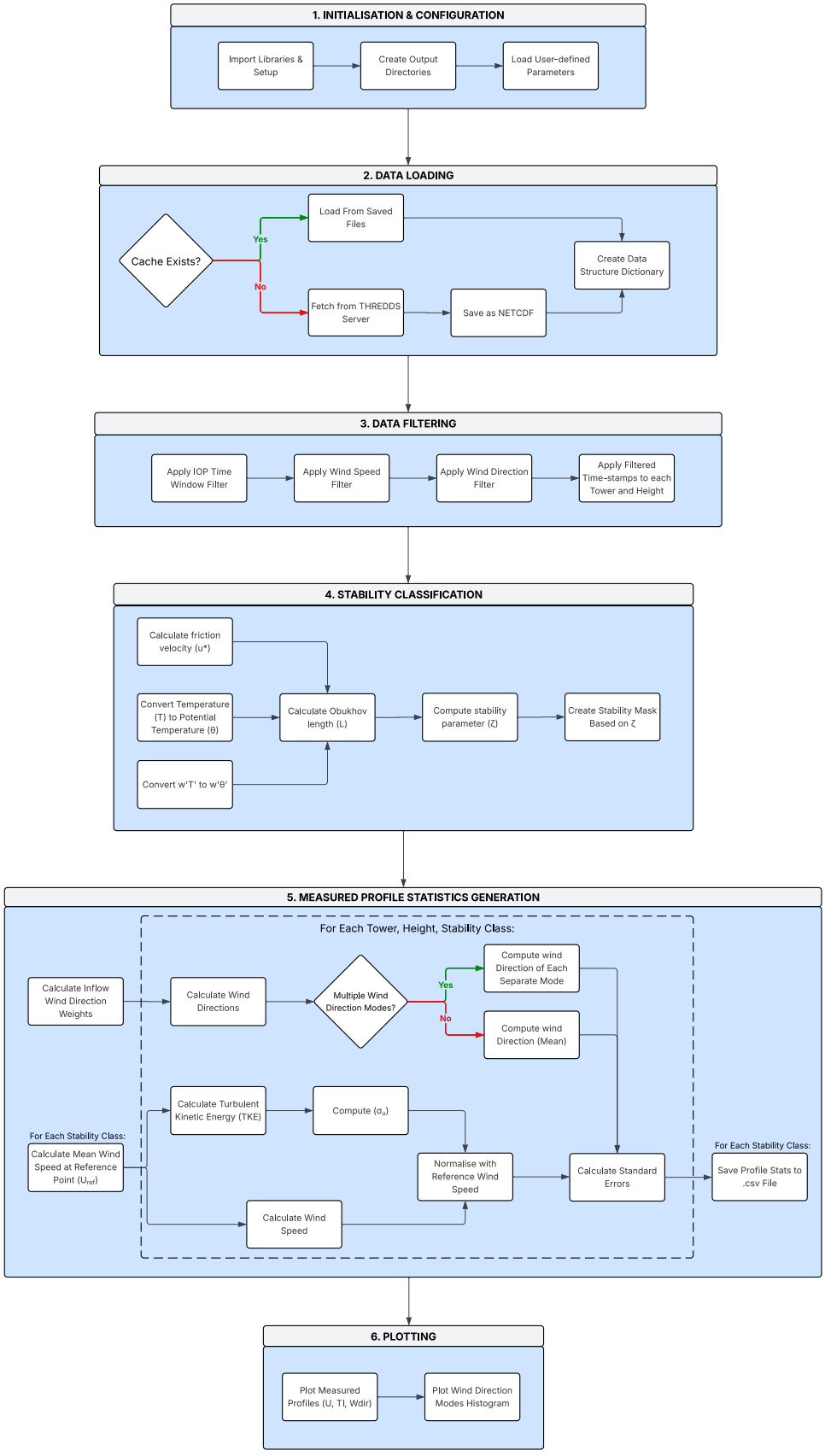

Figure B.2: Data_handling.py flow chart

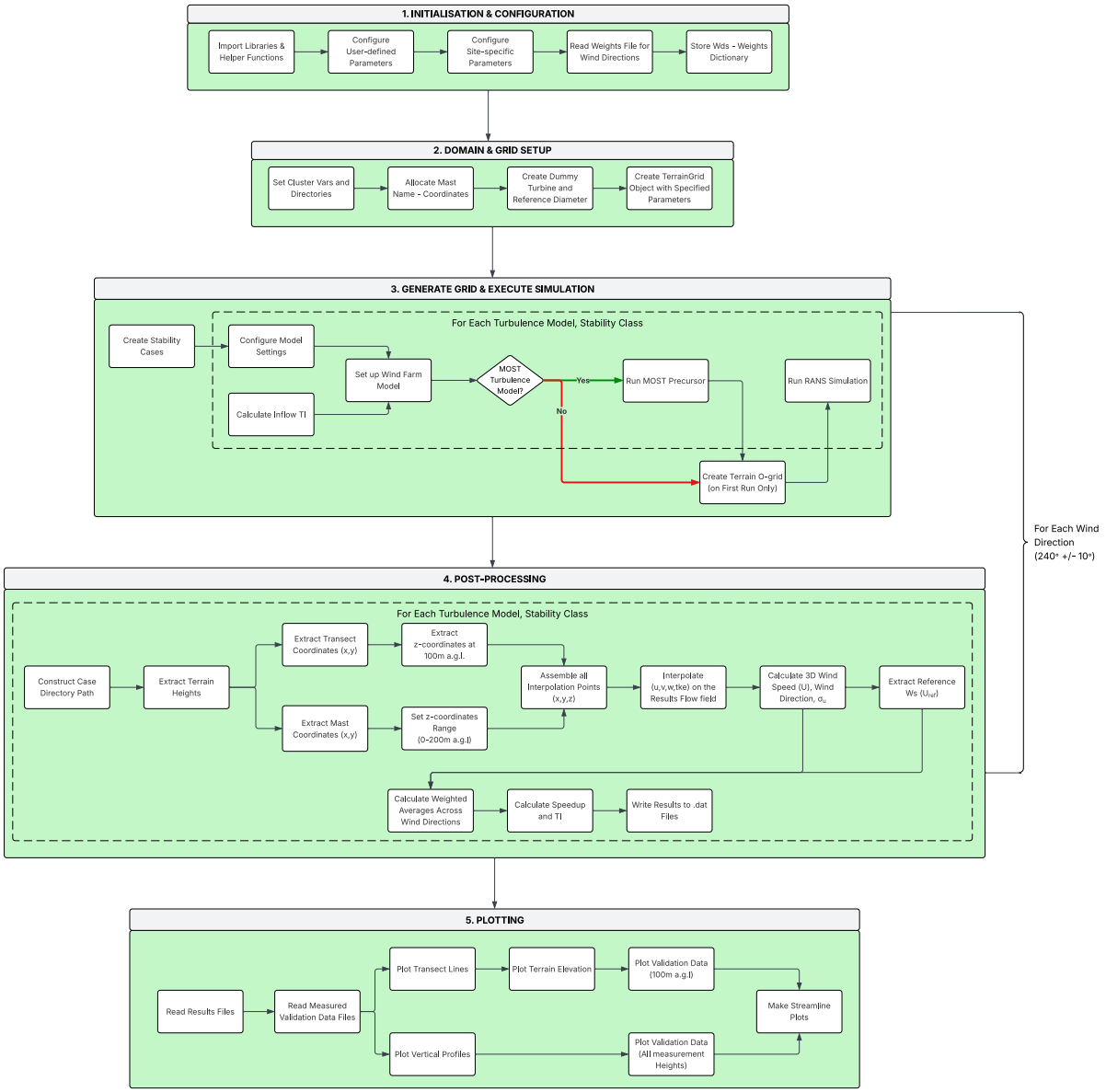

Figure B.3: EllipSys_RANS.py flow chart

BIBLIOGRAPHY

[1] Peter G. Baines. *Topographic Effects in Stratified Flows*. Cambridge, UK: Cambridge University Press, 1998.

[2] R. M. Banta. "Daytime Boundary-Layer Evolution over Mountainous Terrain. Part I: Observations of the Dry Circulations." In: *Monthly Weather Review* 112 (1984), pp. 340–356.

[3] M. Baungaard, M. P. van der Laan, and M. Kelly. "RANS modelling of a single wind turbine wake in the unstable surface layer." In: *Wind Energy Science Discussions* 2021 (2021), pp. 1–29.

[4] A. Bechmann et al. "Recommendations for the use of turbulence models in wind resource assessment." In: *Journal of Physics: Conference Series* 524.1 (2011), p. 012161.

[5] Andreas Bechmann, Niels N. Sørensen, and Jacob Berg. "On the influence of velocity standard deviation in the RIX parameter." In: *Wind Energy* 10.4 (2007), pp. 329–341.

[6] J. Berg, J. Mann, A. Bechmann, M. S. Courtney, and H. E. Jørgensen. "The Bolund Experiment, Part I: Blind Comparison of Microscale Flow Models." In: *Boundary-Layer Meteorology* 141 (2011), pp. 219–243.

[7] J. Berg, N. Troldborg, R. Menke, E. G. Patton, P. P. Sullivan, J. Mann, and N.N. Sørensen. "Flow in complex terrain - a Large Eddy Simulation comparison study." In: *Journal of Physics: Conference Series* 1037.7 (2018), p. 072015.

[8] Bert Blocken, Arne van der Hout, Johan Dekker, and Otto Weiler. "CFD simulation of wind flow over natural complex terrain: Case study with validation by field measurements for Ria de Ferrol, Galicia, Spain." In: *Journal of Wind Engineering and Industrial Aerodynamics* 147 (Dec. 2015), pp. 43–57. DOI: 10.1016/j.jweia.2015.09.007.

[9] J. Blom and L. Wartena. "The Influence of Changes in Surface Roughness on the Development of the Turbulent Boundary Layer in the Lower Layers of the Atmosphere." In: *Journal of Atmospheric Sciences* 26.2 (1969), pp. 255 –265. DOI: 10.1175/1520-0469(1969)026<0255:TIOCIS>2.0.CO;2.

[10] E. Cantero, F. B. Guillén, J. S. Rodrigo, P. A. De Azevedo Santos, J. Mann, N. Vasiljevic, M. Courtney, D. Martínez-Villagrasa, B. Martí, and J. Cuxart. *Alaiz Experiment (ALEX17): Campaign and Data Report: NEWA Deliverable Report D2.21*. NEWA - New European Wind Atlas. 2019. DOI: 10.5281/zenodo.3187482.

[11] E. Cantero, J. Sanz, F. Borbón, D. Paredes, and A. García. "On the measurement of stability parameter over complex mountainous terrain." In: *Wind Energy Science* 7.1 (2022), pp. 221–235. DOI: 10.5194/wes-7-221-2022.

[12] I. P. Castro. "Turbulence characteristics of boundary layers over complex terrain: A review." In: *Boundary-Layer Meteorology* 108 (2003), pp. 1–43.

[13] Y. Chen, F. L. Ludwig, and R. L. Street. "Stable stratification effects on flow and pollutant dispersion through an idealized urban canyon." In: *Journal of Applied Meteorology* 43 (2004), pp. 713–726.

[14] I. L. Coimbra, J. Mann, J. M. L. M. Palma, and V. T. P. Batista. "Exploring dual-lidar mean and turbulence measurements over Perdigão's complex terrain." In: *Atmospheric Measurement Techniques* 18 (2025), pp. 287–303. DOI: 10.5194/amt-18-287-2025.

[15] P. F. Cummins. "Stratified flow over topography: Time-dependent comparisons between model solutions and observations." In: *Dynamics of Atmospheres and Oceans* 32 (2000), pp. 43–72.

[16] Spandan Das. "Numerical verification and systematic sensitivity analysis of RANS modelling for flow over complex terrain." MSc Thesis. MA thesis. Technical University of Denmark (DTU), 2021.

[17] ESA. *Land Cover CCI Product User Guide Version 2*. Technical Report. Available at: https://www.esa-landcover-cci.org/?q=documents. European Space Agency (ESA), 2017.

[18] European Wind Energy Technology Platform. *Strategic Research Agenda and Market Deployment Strategy Synopsis*. Synopsis based on results of TPWind General Assemblies and contributions from members. 2008.

[19] H. J. S. et al. Fernando. "The Perdigão: Peering into Microscale Details of Mountain Winds." In: *Bulletin of the American Meteorological Society* 100.5 (2019), pp. 799–819. DOI: 10.1175/BAMS-D-17-0227.1.

[20] H. J. S. Fernando, B. Verhoef, S. Di Sabatino, L. S. Leo, and S. Park. "The Phoenix Evening Transition Flow Experiment (TRANSFLEX)." In: *Boundary-Layer Meteorology* 156 (2015), pp. 249–269.

[21] Thomas Foken. *Micrometeorology*. Berlin, Germany: Springer, 2006.

[22] S. Gaberšek and D. R. Durran. "Gap flows through idealized topography. Part II: Effects of rotation and surface friction." In: *Journal of the Atmospheric Sciences* 61 (2004), pp. 2846–2862.

[23] J. R. Garratt. *The Atmospheric Boundary Layer*. Cambridge, UK: Cambridge University Press, 1992.

[24] Global Wind Energy Council. *GWEC Global Wind Report 2025*. Accessed June 2025. 2025.

[25] Maryam Golbazi and Cristina L. Archer. "Accuracy of RANS and LES in Simulating Flow over Complex Terrain: Perdigão Case Study." In: *Journal of Physics: Conference Series*. Vol. 1452. 2020, p. 012024. DOI: 10.1088/1742-6596/1452/1/012024.

[26] Andrey A. Grachev, Edgar L. Andreas, Christopher W. Fairall, Peter S. Guest, and Ola P. G. Persson. "Stable boundary-layer regimes from SHEBA observations." In: *Boundary-Layer Meteorology* 116.2 (2005), pp. 201–235.

[27] {Kurt Schaldemose} Hansen, {Rebecca J.} Barthelmie, {Leo E.} Jensen, and Anders Sommer. "The impact of turbulence intensity and atmospheric stability on power deficits due to wind turbine wakes at Horns Rev wind farm." English. In: *Wind Energy* 15.1 (2012), pp. 183–196. ISSN: 1095-4244. DOI: 10.1002/we.512.

[28] J. C. R. Hunt, H. J. S. Fernando, and M. Princevac. "Unsteady Thermally Driven Flows on Gentle Slopes." In: *Journal of the Atmospheric Sciences* 60 (2003), pp. 2169–2182.

[29] Victor S. Indasi, M. Lynch, B. McGann, Frank Yu, F. Jeanneret, and J. Sutton. "WAsP model performance verification using lidar data." In: *International Journal of Energy and Environmental Engineering* 7.1 (2016), pp. 105–113. ISSN: 2251-6832. DOI: 10.1007/s40095-015-0189-6.

[30] International Electrotechnical Commission. *IEC 61400-12-1: Wind turbines – Part 12-1: Power performance measurements of electricity producing wind turbines*. [Online; Accessed 19-February-2025]. Geneva, Switzerland, 2005.

[31] P. S. Jackson and J. C. R. Hunt. "Turbulent Wind Flow Over a Low Hill." In: *Quarterly Journal of the Royal Meteorological Society* 101 (1975), pp. 929–955.

[32] P.A. Jiménez and J. Dudhia. "Improving the Representation of Resolved and Unresolved Topographic Effects on Surface Wind in the WRF Model." In: *Journal of Applied Meteorology and Climatology* 51 (2012), pp. 300–316.

[33] M. P. van der Laan, M. C. Kelly, and N. N. Sørensen. "A new k-epsilon model consistent with Monin-Obukhov similarity theory." In: *Wind Energy* 20.3 (2017), pp. 479–489. DOI: 10.1002/we.2017.

[34] M. P. van der Laan, M. C. Kelly, and N. N. Sørensen. "A new k-epsilon model consistent with Monin-Obukhov similarity theory." In: *Wind Energy* 20.3 (2017), pp. 479–489. DOI: 10.1002/we.2017.

[35] M. P. van der Laan, M. Kelly, M. Baungaard, A. Dicholkar, and E. L. Hodgson. "A simple steady-state inflow model of the neutral and stable atmospheric boundary layer applied to wind turbine wake simulations." In: *Wind Energy Science* 9.10 (2024), pp. 1985–2000. DOI: 10.5194/wes-9-1985-2024.

[36] M. P. van der Laan, N. N. Sørensen, P.-E. Réthoré, J. Mann, M. C. Kelly, N. Troldborg, and E. Machefaux. *PyWakeEllipSys Documentation (Version 5.1)*. Accessed: 2024-12-10. 2024.

[37] M. P. van der Laan, N. N. Sørensen, P.-E. Réthoré, J. Mann, and M. Kelly. "The k-ϵ-f_P model applied to double wind turbine wakes." In: *Journal of Physics: Conference Series* 625 (2015), p. 012162. DOI: 10.1088/1742-6596/625/1/012162.

[38] M. P. van der Laan et al. *PyWakeEllipSys 5.1 documentation*. 2024.

[39] M. Paul van der Laan, Mads Baungaard, and Mark C. Kelly. "Brief communication: A clarification of wake recovery mechanisms." In: *Wind Energy Science* 8.1 (2023), pp. 247–252.

[40] M.P. van der Laan, S.J. Andersen, M. Kelly, and M.C. Baungaard. "Fluid scaling laws of idealized wind farm simulations." In: *Journal of Physics: Conference Series* 1618.6 (2020), p. 062018. DOI: 10.1088/1742-6596/1618/6/062018.

[41] Paul van der Laan and Niels N. Sørensen. *A 1D version of EllipSys*. Tech. rep. E-0141. DTU Wind Energy, 2017.

[42] UCAR/NCAR Earth Observing Laboratory. *Perdigão-ISFS Data Report*. Tech. rep. Accessed: 11 March 2025. National Center for Atmospheric Research, 2017.

[43] Brian Edward Launder and Dudley Brian Spalding. "The numerical computation of turbulent flows." In: *Computer methods in applied mechanics and engineering* 3.2 (1974), pp. 269–289.

[44] Larry Mahrt. "Non-stationary, non-linear and non-local aspects of the stable boundary layer." In: *Boundary-Layer Meteorology* 119 (2006), pp. 1–25.

[45] J. A. Michelsen. *Basis3D - A Platform for Development of Multiblock PDE Solvers*. Tech. rep. Lyngby, Denmark: Technical University of Denmark, 1992.

[46] A.S. Monin and A.M. Obukhov. "Basic laws of turbulent mixing in the surface layer of the atmosphere." In: *Trudy Geofiz. Inst. Akad. Nauk SSSR* 24 (1954), pp. 163–187.

[47] Hans Panofsky and John Dutton. *Atmospheric Turbulence: Models and Methods for Engineering Applications*. Wiley-Interscience, 1984.

[48] S. B. Pope. *Turbulent Flows*. Cambridge University Press, 2000.

[49] C. Rapp and M. Manhart. "Flow over periodic hills: an experimental study." In: *Experiments in Fluids* 51 (2011), pp. 247–269.

[50] Jerome Rowcroft, David Burton, Hugh. M. Blackburn, and John Sheridan. "Siting Wind Turbines Near Cliffs: The Effect of Ruggedness." In: *Journal of Fluids Engineering* 141.3 (Oct. 2018), p. 031104. ISSN: 0098-2202. DOI: 10.1115/1.4041231.

[51] Christopher J. Roy. "Grid Convergence Error Analysis for Mixed-Order Numerical Schemes." In: *AIAA Journal* 41.4 (2003), pp. 595–604.

[52] Salim M. Salim, K. Ong, and S.C. Cheah. "Comparison of RANS, URANS and LES in the Prediction of Airflow and Pollutant Dispersion." In: Jan. 2011.

[53] Z. Sorbjan and A. A. Grachev. "An Evaluation of the Flux–Gradient Relationship in the Stable Boundary Layer." In: *Boundary-Layer Meteorology* 135 (2010), pp. 385–405. DOI: 10.1007/s10546-010-9482-3.

[54] R. B. Stull. *An Introduction to Boundary Layer Meteorology*. Vol. 13. Atmospheric and Oceanographic Sciences Library. Springer Netherlands, 1988. DOI: 10.1007/978-94-009-3027-8.

[55] J. N. Sørensen. "General Purpose Flow Solver Applied to Flow Over Hills." PhD thesis. Roskilde, Denmark: Technical University of Denmark, 1995.

[56] N. N. Sørensen, A. Bechmann, J. Johansen, L. Myllerup, P. Botha, S. Vinther, and B. S. Nielsen. "Identification of severe wind conditions using a Reynolds Averaged Navier-Stokes solver." In: *Journal of Physics: Conference Series* 75 (2007), p. 012053. DOI: 10.1088/1742-6596/75/1/012053.

[57] P. A. Taylor and H. W. Teunissen. *The Askervein Hill Project: Report on the Sept./Oct. 1983 Main Field Experiment*. Technical Report MSRB-84-6. Downsview, Ontario: Atmospheric Environment Service, 1984.

[58] I. Troen and E. L. Petersen. *European Wind Atlas*. Roskilde, Denmark: Risø National Laboratory, 1989, p. 656. ISBN: 87-550-1482-8.

[59] C. D. Whiteman. *Observations of Thermally Developed Wind Systems in Mountainous Terrain*. Berlin, Heidelberg: Springer, 1990.

[60] C. D. Whiteman. *Mountain Meteorology: Fundamentals and Applications*. New York, USA: Oxford University Press, 2000.

[61] Kjell Zum Berge, Annika Gaiser, Hermann Knaus, Andreas Platis, and Jens Bange. "Seasonal Changes in Boundary-Layer Flow Over a Forested Escarpment Measured by an Uncrewed Aircraft System." In: *Boundary-Layer Meteorology* 186 (Sept. 2022). DOI: 10.1007/s10546-022-00743-4.

[62] Julia Lange et al. "For wind turbines in complex terrain, the devil is in the detail." English. In: *Environmental Research Letters* 12.9 (2017). ISSN: 1748-9326. DOI: 10.1088/1748-9326/aa81db.